Implicit dynamic buckling analysis of thin-shell isogeometric structures considering geometric imperfections

Yujie Guo[1]* Maodong Pan[2] Xiaohui Wei[1] Fei Luo[1] Fangbin Sun[1] Martin Ruess[3]

[1] *College of Aerospace Engineering, Nanjing University of Aeronautics and Astronautics, Nanjing, China*
[2] *College of Mathematics, Nanjing University of Aeronautics and Astronautics, Nanjing, China*
[3] *Department of Mechanical and Process Engineering, Düsseldorf University of Applied Sciences, Düsseldorf, Germany*

SUMMARY

In continuation of our previous work on nonlinear stability analysis of trimmed isogeometric thin shells, this contribution is an extension to dynamic buckling analyses for predicting reliably complex snap-through and mode-jumping behavior. Specifically, a modified generalized-α time integration scheme is used and combined with a nonlinear isogeometric Kirchhoff-Love shell element to provide second-order accuracy while introducing controllable high-frequency dissipation. In addition, a weak enforcement of essential boundary conditions based on a penalty approach is considered with a particular focus on the inhomogeneous case of imposed prescribed displacements. Moreover, we propose a least-squares B-spline surface fitting approach and corresponding error measures to model both eigenmode based and measured geometric imperfections. The imperfect geometries thus obtained can be naturally integrated into the framework of isogeometric nonlinear dynamic shell analysis. Based on this idea, the different modeling methods and the influence of the appropriately considered geometric imperfections on the dynamic buckling behavior can be investigated systematically. Both perfect and geometrically imperfect shell models are considered to assess the performance of the proposed method. We compare our method with established developments in this field and demonstrate superior achievements with regard to solution quality and robustness.
Copyright © 0000 John Wiley & Sons, Ltd.

CONTENTS

---

*Correspondence to: yujieguo@nuaa.edu.cn

1. INTRODUCTION

Shells are prone to buckling. Comparing experiments and theoretical predictions, the buckling loads of thin-walled structures show large discrepancies and scatters [1, 2, 3], which can be traced back largely to combined effects of nonlinearity and randomness of different sources of imperfections [4, 5, 6, 7, 8]. Among the different types of imperfections, geometric imperfections, mainly due to manufacturing processes, are ubiquitous with severe effects on the buckling behavior of shell structures. This observation has led to a number of studies on the geometric imperfection sensitivity of thin-walled structures using experiments [4, 9, 10], different buckling theories [11, 12] as well as numerical approaches [6, 13, 14, 15, 16] to capture this phenomena appropriately. The finite element method (FEM) as the established numerical standard in this field of research uses linear facet elements to represent mostly curved shell geometries. This approximation introduces additional geometric imperfections to what should be a smoothly curved structure which may lead to accuracy problems in shell buckling analysis [17].

In recent years, isogeometric analysis (IGA) [17] has attracted a considerable amount of attention in the field of shell analysis due to the higher-order smooth geometry representation and higher-order approximation of physical fields. A number of IGA shell elements [18, 19, 20, 21, 22, 23, 24, 25, 26, 27, 28] have been proposed which show superior approximation properties compared to traditional FE shell elements. In particular, the higher-order continuous approximation basis used allows straightforward construction of rotation-free Kirchhoff-Love shell elements, for which fast convergence has been demonstrated in both linear and nonlinear cases. Despite the success of isogeometric shell analysis, the non-interpolatory property of NURBS still remains a challenge for the enforcement of essential boundary conditions and multi-patch coupling constraints, especially along trimmed patch boundaries. To cope with this challenge, three major strategies are currently well established in isogeometric analysis including (i) penalty methods [29, 30, 31, 32], (ii) Lagrange multiplier and augmented Lagrange multiplier methods [33, 34, 26], and (iii) Nitsche-like methods [35, 36, 37, 38, 39, 40, 41, 42, 43]. An overview and comparison of the different strategies is presented in [44].

The advent of IGA has initiated a number of researches in the field of shell buckling, where the property of accurate geometry representation is advantageously exploited. These researches can be classified into two categories: static buckling analysis [45, 46, 47, 48, 49, 50, 51, 52, 53, 15]

and dynamic buckling analysis [54, 55, 56, 57]. In linear static buckling analysis, the superior accuracy of IGA in terms of buckling loads and mode shapes has been frequently observed [45, 46]. In particular, *Oesterle et al.* [51] systematically investigated the sources of the observed superior accuracy and demonstrated an irreplaceable role of high approximation power of k-refined NURBS rather than the exact geometry representation. However, effects of nonlinearity and geometric imperfections have not been considered. In nonlinear static buckling analysis, where snap-through or bifurcation exists, a path-following method is indispensable to trace the post-buckling equilibrium path [53, 15, 49]. To this end, a computationally highly efficient reduced order method, the Koiter-Newton arc-length method, was developed in [14] and later used in the framework of isogeometric analysis to study buckling of thin shell structures [53, 15].

In some cases, it is difficult to compute the complete shell buckling behavior by path-following methods due to complex mode jumps and branch-switching [58, 59]. Alternatively, one can analyze shell buckling problems using quasi-static methods, such as dynamic relaxation, or by dynamic methods, such as explicit shell dynamics [60, 61, 62, 63, 55, 57]. A less common approach to analyzing shell buckling are implicit dynamics schemes, although they are more stable and allow much larger time steps compared to explicit schemes [64]. Typical implicit schemes for structural dynamics are representatives of the Newmark family [65], where second-order accuracy can be preserved with the Newmark parameters $\beta = 0.25, \gamma = 0.5$. However, sometimes it is desirable to introduce high-frequency damping in shell buckling analysis to mitigate the influences of the inaccurate high-frequency modes. To introduce numerical dissipation, the Newmark schemes will drop to first-order accuracy which motivated the development of second-order accurate, high-frequency dissipative, one-step implicit schemes, e.g. HHT-α [66], Bossak [67] and generalized-α schemes [68]. These schemes compute inertial, external and internal forces as a linear combination of corresponding quantities at both ends of the time step. Unfortunately, when applied to nonlinear elastodynamics, the above conservation/dissipation properties are not preserved [69]. To solve this problem, an energy and momentum preserving scheme [70, 71, 72, 73, 74] was proposed, which combines the midpoint rule and the algorithmic evaluation of stresses and ensures second order accuracy in nonlinear structural dynamics. Furthermore, to introduce high-frequency dissipation, a mid-point rule in the above energy-momentum conserving scheme was replaced with the generalized-α scheme leading to the generalized energy-momentum scheme [72, 75]. Special cases are the modified generalized-α, HHT-α and Bossak schemes, etc. Although conservation of momentum is not guaranteed, the generalized energy-momentum scheme is considered to be highly suitable for nonlinear structural dynamic analysis [76]. Other recently developed implicit schemes which are not considered herein can be found in [77, 78, 79, 56].

In the present paper, we extend our previous work on nonlinear stability analysis of trimmed isogeometric thin shells to dynamic analyses to allow for an efficient prediction of complex snap-through and mode jumping behavior. Specifically, a modified generalized-α time integration scheme is used and combined with the nonlinear isogeometric Kirchhoff-Love shell element to ensure second-order accuracy while introducing controllable high-frequency dissipation. Besides, a penalty-based weak enforcement of essential boundary conditions is tested extensively, with a particular focus on the non-homogeneous case of prescribed displacements. Moreover, we propose a least-squares B-spline surface fitting approach and corresponding error measures to model both, eigenmode based and measured geometric imperfections. The obtained imperfect geometries can be naturally incorporated into the framework of isogeometric nonlinear shell dynamic analysis. Based on this idea, the influences of the geometric imperfection and the modeling methods of geometric imperfection on the dynamic buckling behavior of shell structures is investigated systematically.

The paper is organized as follows: the Kirchhoff-Love shell theory, governing equations including an isogeometric discretization is summarized briefly in Section 2. Next, the generalized-α time integration scheme and the corresponding linearization steps are presented in Section 3. We present and discuss the weak enforcement of homogeneous and non-homogeneous essential boundary conditions for a Kirchhoff-Love shell formulation in Section 4. Furthermore, a least-squares B-spline surface fitting approach for the modeling of geometric imperfections is introduced in Section 5. Various numerical examples are presented in Section 6 to document and assess carefully the

developed advancements. Finally, we summarize the main findings and draw conclusions in Section 7.

2. ISOGEOMETRIC KIRCHHOFF-LOVE SHELL ELEMENT FORMULATION

In the following, we provide a brief summary of the used isogeometric Kirchhoff-Love shell element. In sub-section 2.1 the kinematic assumptions and constitutive relations are summarized. In sub-section 2.2, we present the governing integral equations and corresponding isogeometric discretization.

2.1. Kinematics and constitutive relations

Herein, Kirchhoff-Love assumptions are used to model thin shells where transverse shear and normal deformations are neglected. Therefore, the director of the shell remains normal to the mid-surface during deformation, and the description of the shell kinematics can be purely represented by the mid-surface. In the following, we use an upper case notation for quantities which refer to the undeformed reference configuration, and a lower case notation for quantities which refer to the current deformed configuration. We note that, Greek indices take values $1, 2$, Latin indices take values $1, 2, 3$.
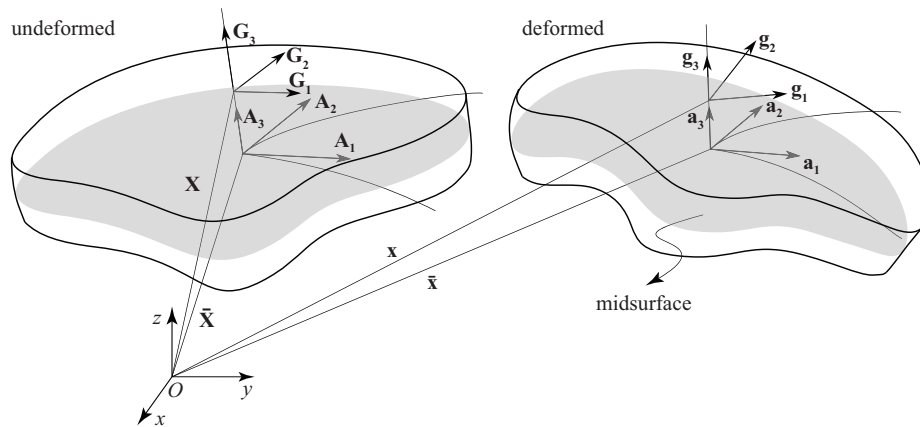

Figure 1. Shell geometry and coordinate systems.

The reference and current configurations of the 3D shell body, cf. Figure 1, can be described as:

$$\mathbf{X}(\xi_1, \xi_2, \xi_3) = \bar{\mathbf{X}}(\xi_1, \xi_2) + \xi_3 \, \mathbf{D}(\xi_1, \xi_2), \tag{1}$$

$$\mathbf{x}(\xi_1, \xi_2, \xi_3) = \bar{\mathbf{x}}(\xi_1, \xi_2) + \xi_3 \, \mathbf{d}(\xi_1, \xi_2), \tag{2}$$

where $\mathbf{X}$ and $\mathbf{x}$ are the position vectors of a material point in the reference and current configuration respectively, $\bar{\mathbf{X}}$ and $\bar{\mathbf{x}}$ denote the position vectors of the shell mid-surface, $\mathbf{D}$ and $\mathbf{d}$ are the directors of the shell mid-surface, where ξ_i denotes the parameterized coordinates of the shell, and $\xi_3 \in [-0.5h, 0.5h]$ varies linearly through the shell thickness h. Based on the above description, the displacement of each point of the shell body can be represented as $\mathbf{u} = \mathbf{x} - \mathbf{X}$.

The basis vectors of the shell midsurface are defined as:

$$\mathbf{A}_\alpha = \bar{\mathbf{X}}_{,\alpha}, \qquad \mathbf{A}_3 = \mathbf{D} = \frac{\mathbf{A}_1 \times \mathbf{A}_2}{|\mathbf{A}_1 \times \mathbf{A}_2|}, \tag{3}$$

$$\mathbf{a}_\alpha = \bar{\mathbf{x}}_{,\alpha}, \qquad \mathbf{a}_3 = \mathbf{d} = \frac{\mathbf{a}_1 \times \mathbf{a}_2}{|\mathbf{a}_1 \times \mathbf{a}_2|} \tag{4}$$

where $(\cdot)_{,\alpha}$ denotes the partial derivative $\partial(\cdot)/\partial\xi_\alpha$. With (3) and (4), the covariant base vectors can be described as:

$$\mathbf{G}_\alpha \;=\; \mathbf{X}_{,\alpha} \;=\; \bar{\mathbf{X}}_{,\alpha} + \xi_3\mathbf{D}_{,\alpha} \;=\; \mathbf{A}_\alpha + \xi_3\mathbf{D}_{,\alpha}, \qquad \mathbf{G}_3 \;=\; \mathbf{X}_{,3} \;=\; \mathbf{D}, \qquad (5)$$

$$\mathbf{g}_\alpha \;=\; \mathbf{x}_{,\alpha} \;=\; \bar{\mathbf{x}}_{,\alpha} + \xi_3\mathbf{d}_{,\alpha} \;=\; \mathbf{a}_\alpha + \xi_3\mathbf{d}_{,\alpha}, \qquad \mathbf{g}_3 \;=\; \mathbf{x}_{,3} \;=\; \mathbf{d}. \qquad (6)$$

The Green-Lagrange strain tensor $\mathbf{E}$ follows as:

$$\mathbf{E} \;=\; \frac{1}{2}\left(\mathbf{F}^{\mathrm{T}}\mathbf{F} - \mathbf{I}\right) \;=\; E_{ij}\mathbf{G}^i \otimes \mathbf{G}^j \qquad (7)$$

where $\mathbf{F} = \frac{d\mathbf{x}}{d\mathbf{X}}$ is the deformation gradient which links the reference configuration to the deformed configuration and $\mathbf{I}$ is the identity tensor. The strain tensor coefficients in (7) are defined as:

$$E_{ij} \;=\; \frac{1}{2}(g_{ij} - G_{ij}) \qquad (8)$$

where

$$g_{ij} \;=\; \mathbf{g}_i \cdot \mathbf{g}_j, \qquad G_{ij} \;=\; \mathbf{G}_i \cdot \mathbf{G}_j. \qquad (9)$$

For the geometrically nonlinear elastic Kirchhoff-Love shell, the director is assumed to be non-stretchable and remains straight and normal to the midsurface during deformation. Therefore, the transverse shear and normal strains vanish, $E_{\alpha3} = E_{33} = 0$. Substituting (5) and (6) into (9) and neglecting second order terms results in:

$$E_{\alpha\beta} \;=\; \varepsilon_{\alpha\beta} + \theta_3\kappa_{\alpha\beta} \qquad (10)$$

$$=\; \frac{1}{2}\left[(\mathbf{a}_\alpha \cdot \mathbf{a}_\beta - \mathbf{A}_\alpha \cdot \mathbf{A}_\beta) + 2\xi_3\left(\mathbf{A}_{\alpha,\beta} \cdot \mathbf{D} - \mathbf{a}_{\alpha,\beta} \cdot \mathbf{d}\right)\right] \qquad (11)$$

where $\varepsilon_{\alpha\beta}$ and $\kappa_{\alpha\beta}$ are the membrane and bending strains, respectively, where we have used the relations $\mathbf{A}_{\alpha,\beta} \cdot \mathbf{D} = -\mathbf{A}_\alpha \cdot \mathbf{D}_{,\beta}$, and where

$$\mathbf{A}_{\alpha,\beta} \;=\; \mathbf{X}_{\alpha,\beta}, \qquad \mathbf{a}_{\alpha,\beta} \;=\; \mathbf{x}_{\alpha,\beta}. \qquad (12)$$

The relation between stress and strain tensor for the plane stress problem are established using the St. Venant-Kirchhoff constitutive model which is in Voigt notation:

$$\begin{bmatrix} \bar{S}^{12} \\ \bar{S}^{22} \\ \bar{S}^{12} \end{bmatrix} \;=\; \bar{\mathbf{C}}\begin{bmatrix} \bar{E}_{12} \\ \bar{E}_{22} \\ 2\bar{E}_{12} \end{bmatrix} \;=\; \frac{E}{1-\nu^2}\begin{bmatrix} 1 & \nu & 0 \\ \nu & 1 & 0 \\ 0 & 0 & \frac{1-\nu}{2} \end{bmatrix}\begin{bmatrix} \bar{E}_{12} \\ \bar{E}_{22} \\ 2\bar{E}_{12} \end{bmatrix} \qquad (13)$$

where $S^{\alpha\beta}$ is the contravariant components of the second Piola-Kirchhoff stress tensor $\mathbf{S}$, where $\mathbf{C}$ is the material tensor, where E is Young's modulus and ν the Poisson ratio, where $(\bar{\cdot})$ denotes the quantities represented in the local Cartesian coordinate system $\mathbf{e}_\gamma \otimes \mathbf{e}_\delta$. A transformation of the strain components from the contravariant basis to the local Cartesian basis follows as:

$$\bar{E}_{\gamma\delta} \;=\; E_{\alpha\beta}(\mathbf{e}_\gamma \cdot \mathbf{G}^\alpha)(\mathbf{G}^\beta \cdot \mathbf{e}_\delta) \qquad (14)$$

For Kirchhoff-Love shell problems, the membrane force $\bar{N}^{\alpha\beta}$ and bending moments $\bar{M}^{\alpha\beta}$ are utilized which result from the integration of the stress components through the shell thickness:

$$\begin{bmatrix} \bar{N}^{11} \\ \bar{N}^{22} \\ \bar{N}^{12} \end{bmatrix} \;=\; h \cdot \bar{\mathbf{C}}\begin{bmatrix} \bar{\varepsilon}_{11} \\ \bar{\varepsilon}_{22} \\ 2\bar{\varepsilon}_{12} \end{bmatrix}, \qquad (15)$$

and

$$\begin{bmatrix} \bar{M}^{11} \\ \bar{M}^{22} \\ \bar{M}^{12} \end{bmatrix} \;=\; \frac{h^3}{12} \cdot \bar{\mathbf{C}}\begin{bmatrix} \bar{\kappa}_{11} \\ \bar{\kappa}_{22} \\ 2\bar{\kappa}_{12} \end{bmatrix}. \qquad (16)$$

2.2. Governing equations and isogeometric discretizations

The governing integral equations of the geometrically nonlinear elastic Kirchhoff-Love shell formulation are:

$$\int_A \mathbf{P}_0 \cdot \delta\mathbf{u}\, dA + \int_{\Gamma_t} \mathbf{T}_0 \cdot \delta\mathbf{u}\, d\Gamma - \int_A (\mathbf{N} : \delta\varepsilon + \mathbf{M} : \delta\kappa) dA \quad = \quad \int_A \rho h \ddot{\mathbf{u}} \cdot \delta\mathbf{u}\, dA \quad (17)$$

where $\delta\varepsilon$, $\delta\kappa$ and $\delta\mathbf{u}$ denote the variation of the membrane strain, bending strain and displacement, respectively, where A and dA are the analysis domain and differential area of the shell midsurface in the reference configuration, respectively, where ρ is the density, $\mathbf{P}_0$ is the unit surface load and $\mathbf{T}_0$ is the prescribed traction along the Neumann boundary Γ_t. For simplicity, we assume $\mathbf{P}_0$ and $\mathbf{T}_0$ are independent of the displacement field $\mathbf{u}$. The upper double dots in the term on the right hand-side of (17) which represents the inertia forces denote the second derivative of $\mathbf{u}$ with respect to time. It should be noted that we neglected the actual damping in (17) in order to study the influence of the numerical damping of the time integration method on the dynamic buckling behaviors of the shell structures.

Following the concept of isogeometric analysis, the displacement field and its variations are discretized with the same NURBS basis used to describe the shell midsurface $\bar{\mathbf{X}}$:

$$\bar{\mathbf{X}} \quad = \quad \sum_{i=1}^{n} R_i \mathbf{P}_i \quad = \quad \mathbf{R}^{\mathrm{T}}\mathbf{P} \quad (18)$$

$$\mathbf{u} \quad = \quad \sum_{i=1}^{n} R_i \mathbf{U}_i \quad = \quad \mathbf{R}^{\mathrm{T}}\mathbf{U} \quad (19)$$

$$\delta\mathbf{u} \quad = \quad \sum_{i=1}^{n} R_i \delta\mathbf{U}_i \quad = \quad \mathbf{R}^{\mathrm{T}}\delta\mathbf{U}. \quad (20)$$

where n is the total number of control points, where vectors $\mathbf{U}_i$ and $\delta\mathbf{U}_i$ represent sets of three unknown coefficients associated with each control point $\mathbf{P}_i$, where $R_i = R_i(\xi_1, \xi_2)$ is the i-th NURBS basis function, where $\mathbf{R}$, $\mathbf{P}$, $\mathbf{U}$ and $\delta\mathbf{U}$ are the vectors collecting the corresponding quantities. The two-dimensional NURBS basis functions of order $p = (p_1, p_2)$ in the ξ_1 and ξ_2 parametric directions are defined as:

$$R_{i,p}(\xi_1, \xi_2) = \frac{N_{k,p_1}(\xi_1)\, M_{l,p_2}(\xi_2)\, w_{kl}}{\sum_{\hat{k}=1}^{n_1} \sum_{\hat{l}=1}^{n_2} N_{\hat{k},p_1}(\xi_1)\, M_{\hat{l},p_2}(\xi_2)\, w_{\hat{k}\hat{l}}} \quad (21)$$

where $i = i(k, l)$ represents a mapping between the two dimensional tensor product index space (k, l) and the one dimensional index space i, where $N_{k,p_1}(\xi_1)$ and $M_{l,p_2}(\xi_2)$ are the one-dimensional B-spline basis of polynomial degree p_s in each parametric direction with $s \in 1, 2$, respectively, where w_{kl} are the weights associated to the $i = i(k, l)$-th NURBS basis. For simplicity, we use i instead of $i(k, l)$ and omit the parametric coordinates ξ_1 and ξ_2 in the following of the paper. For more details of the NURBS and B-spline basis functions, we refer the reader to [80].

Substituting (19) and (20) into (17) and leveraging the arbitrary nature of $\delta\mathbf{U}_i$, semi-discretized equilibrium equations can be obtained:

$$\mathbf{f} - \mathbf{r} \quad = \quad \mathbf{M}_a \ddot{\mathbf{U}} \quad (22)$$

where $\mathbf{M}_a$ is the mass matrix denoted as:

$$\mathbf{M}_a \quad = \quad \int_A \rho h \mathbf{R}^T \mathbf{R}\, dA\,, \quad (23)$$

where $\mathbf{r}$ and $\mathbf{f}$ in (22) are the internal and external force vectors, respectively, expressed as:

$$\mathbf{r} \quad = \quad \int_A \left(\mathbf{N} : \frac{\partial\varepsilon}{\partial\mathbf{U}} + \mathbf{M} : \frac{\partial\kappa}{\partial\mathbf{U}} \right) dA \quad (24)$$

$$\mathbf{f} \quad = \quad \int_A \mathbf{R}^T \cdot \mathbf{P}_0 \, dA + \int_{\Gamma_t} \mathbf{R}^T \cdot \mathbf{T}_0 \, d\Gamma \, . \tag{25}$$

3. GENERALIZED-α TIME MARCHING SCHEME

In this section, the modified generalized-α time marching scheme used to discretize the time domain of the governing equations is briefly introduced in 3.1. Then a linearization and iterative solution strategy of the governing equations is presented in 3.2.

3.1. Algorithmic equations

In general, equation (22) represents a time-dependent nonlinear problem and can be solved for each time step with iterative procedures to ensure a balance of momentum. Assume that the time interval of interest $[0, T]$ is partitioned into typical time intervals $[t_n, t_{n+1}]$ with the corresponding time step $\Delta t = t_{n+1} - t_n$, and that the state variables are known at the time t_n. The integration of Eq. (22) is then restricted to successively solving the state variables at the end of each step t_{n+1}.

Assuming Newmark's approximations, the acceleration is assumed to be linearly changing over the time step which results for velocities and displacements in:

$$\dot{\mathbf{U}}_{n+1} \quad = \quad \dot{\mathbf{U}}_n + (1-\gamma)\Delta t \, \ddot{\mathbf{U}}_n + \gamma \Delta t \, \ddot{\mathbf{U}}_{n+1} \tag{26}$$

$$\mathbf{U}_{n+1} \quad = \quad \mathbf{U}_n + \Delta t \, \dot{\mathbf{U}}_n + \frac{1-2\beta}{2} \Delta t^2 \ddot{\mathbf{U}}_n + \beta \, \Delta t^2 \ddot{\mathbf{U}}_{n+1} \tag{27}$$

where β and γ are the integration parameters which determine the characteristics of the system. Consequently, the accelerations and velocities at the end of the time step are:

$$\ddot{\mathbf{U}}_{n+1} \quad = \quad \frac{1}{\beta \Delta t^2} \left(\mathbf{U}_{n+1} - \mathbf{U}_n \right) - \frac{1}{\beta \Delta t} \dot{\mathbf{U}}_n - \frac{1-2\beta}{2\beta} \ddot{\mathbf{U}}_n \tag{28}$$

$$\dot{\mathbf{U}}_{n+1} \quad = \quad \frac{\gamma}{\beta \Delta t} \left(\mathbf{U}_{n+1} - \mathbf{U}_n \right) - \frac{\gamma - \beta}{\beta} \dot{\mathbf{U}}_n - \frac{\gamma - 2\beta}{2\beta} \Delta t \, \ddot{\mathbf{U}}_n \, . \tag{29}$$

Following [72], the semi-discrete governing equation (22) is applied to general mid-points $t_{n+1-\alpha_f}$ and $t_{n+1-\alpha_m}$ instead of the end-points t_{n+1} of the time step interval which modifies the governing equations to:

$$\mathbf{f}_{n+1-\alpha_f} - \mathbf{r}_{n+1-\alpha_f} \quad = \quad \mathbf{M}_a \, \ddot{\mathbf{U}}_{n+1-\alpha_m} \tag{30}$$

where the subscripts represent the time discrete combinations of the corresponding quantities expressed as:

$$\ddot{\mathbf{U}}_{n+1-\alpha_m} \quad = \quad (1-\alpha_m)\ddot{\mathbf{U}}_{n+1} + \alpha_m \ddot{\mathbf{U}}_n \tag{31}$$

$$\mathbf{f}_{n+1-\alpha_f} \quad = \quad (1-\alpha_f)\mathbf{f}_{n+1} + \alpha_f \mathbf{f}_n \tag{32}$$

and where $\mathbf{r}_{n+1-\alpha_f}$ is the algorithmic internal forces evaluated at the generalized mid-point $t_{n+1-\alpha_f}$. Classically, the internal force is represented accordingly:

$$\mathbf{r}_{n+1-\alpha_f} \quad = \quad (1-\alpha_f)\mathbf{r}_{n+1} + \alpha_f \mathbf{r}_n \quad = \quad (1-\alpha_f)\mathbf{r}(\mathbf{U}_{n+1}) + \alpha_f \mathbf{r}(\mathbf{U}_n) \, . \tag{33}$$

Alternatively, $\mathbf{r}_{n+1-\alpha_f}$ can be represented as:

$$\mathbf{r}_{n+1-\alpha_f} \quad = \quad \mathbf{r}(\mathbf{U}_{n+1-\alpha_f}) \tag{34}$$

where

$$\mathbf{U}_{n+1-\alpha_f} \quad = \quad (1-\alpha_f)\mathbf{U}_{n+1} + \alpha_f \mathbf{U}_n \, . \tag{35}$$

Unless otherwise announced, we use the algorithmic internal force (34) in the following.

The choice of the algorithmic parameters α_f, α_m, β and γ is crucial for the stability and accuracy of the generalized-α scheme. In principle, these parameters are functions of the spectral radius $\rho_\infty \in [0, 1]$ which represents the spectral radius of the amplification matrix of the recurrence algorithm when $(\Delta t / T) \to \infty$ with T being the time period [68]:

$$\alpha_m = \frac{2\rho_\infty - 1}{\rho_\infty + 1}, \quad \alpha_f = \frac{\rho_\infty}{\rho_\infty + 1}, \quad \beta = \frac{1}{(1 + \rho_\infty)^2}, \quad \gamma = \frac{3 - \rho_\infty}{2(1 + \rho_\infty)}. \quad (36)$$

The value of ρ_∞ controls the amount of high-frequency numerical dissipation where $\rho_\infty = 1$ corresponds to the case of no dissipation, while $\rho_\infty = 0$ corresponds to the case of asymptotic annihilation.

Combining the modified governing equation (30) and the Newmark approximations (28), (29), the effective structural equation can be derived as:

$$\mathbf{r}(\mathbf{U}_{n+1-\alpha_f}) + \mathbf{M}_a \left(\frac{1 - \alpha_m}{\beta \Delta t^2}(\mathbf{U}_{n+1} - \mathbf{U}_n) - \frac{1 - \alpha_m}{\beta \Delta t}\dot{\mathbf{U}}_n - \frac{1 - \alpha_m - 2\beta}{2\beta}\ddot{\mathbf{U}}_n \right)$$
$$- \mathbf{f}_{n+1-\alpha_f} = \mathbf{G}(\mathbf{U}_{n+1}) = \mathbf{0} \quad (37)$$

where $\mathbf{G}(\mathbf{U}_{n+1})$ is the nonlinear residual vector which depends on the unknown displacement $\mathbf{U}_{n+1}$.

3.2. Linearization and iterative solution procedure

The consistent linearization of the nonlinear residual $\mathbf{G}(\mathbf{U}_{n+1})$ in (37) reads:

$$\mathbf{G}(\mathbf{U}_{n+1}^{k+1}) = \mathbf{G}(\mathbf{U}_{n+1}^k) + \frac{\partial \mathbf{G}(\mathbf{U}_{n+1}^k)}{\partial \mathbf{U}_{n+1}}(\mathbf{U}_{n+1}^{k+1} - \mathbf{U}_{n+1}^k) + \mathcal{O}(\Delta t^2) = \mathbf{0} \quad (38)$$

where the superscripts k and $k + 1$ represent the relevant iteration cycles in each time step.

Substituting (37) into (38) and taking derivatives w.r.t. the displacement variables $\mathbf{U}_{n+1}$ results in the linear system of equations:

$$\mathbf{K}_* \, \Delta \mathbf{U}_{n+1}^{k+1} = -\mathbf{G}(\mathbf{U}_{n+1}^k) \quad (39)$$

where $\Delta \mathbf{U}_{n+1}^{k+1} = \mathbf{U}_{n+1}^{k+1} - \mathbf{U}_{n+1}^k$ is the iterative change of the displacement vector, and where $\mathbf{K}_*$ is the effective stiffness matrix of form:

$$\mathbf{K}_* = \frac{\partial \mathbf{r}(\mathbf{U}_{n+1-\alpha_f}(\mathbf{U}_{n+1}^k))}{\partial \mathbf{U}_{n+1}} + \frac{1 - \alpha_m}{\beta \Delta t^2}\mathbf{M}_a = (1 - \alpha_f)\mathbf{K}_T + \frac{1 - \alpha_m}{\beta \Delta t^2}\mathbf{M}_a \quad (40)$$

where $\mathbf{K}_T = \mathbf{K}_T(\mathbf{U}_{n+1-\alpha_f}(\mathbf{U}_{n+1}^k))$ is the deformation dependent algorithmic tangent stiffness matrix expressed as:

$$\mathbf{K}_T = \int_A \left(\frac{\partial \mathbf{N}}{\partial \mathbf{U}} \cdot \frac{\partial \boldsymbol{\varepsilon}}{\partial \mathbf{U}} + \mathbf{N} \cdot \frac{\partial^2 \boldsymbol{\varepsilon}}{\partial \mathbf{U} \partial \mathbf{U}} + \frac{\partial \mathbf{M}}{\partial \mathbf{U}} \cdot \frac{\partial \boldsymbol{\kappa}}{\partial \mathbf{U}} + \mathbf{M} \cdot \frac{\partial^2 \boldsymbol{\kappa}}{\partial \mathbf{U} \partial \mathbf{U}} \right) dA. \quad (41)$$

Equation (39) can be solved iteratively applying a Newton-Raphson method. At each new time step the displacement field $\mathbf{U}_{n+1}^0$ is set to the converged state of the previous time step as an appropriate initial guess of the iteration. Based on the first estimation of displacement increment $\Delta \mathbf{U}_{n+1}^1$, the internal force vector, the stiffness matrix as well as the accelerations for the next iteration is updated. A detailed step-by-step representation of the generalized-α algorithm is presented in Algorithm 1.

Algorithm 1 Generalized-α time integration algorithm for nonlinear problems

---

1: **Initialize:** $\mathbf{U}_{t=0}$, $\dot{\mathbf{U}}_{t=0}$ and $\mathbf{r}_{t=0}$
2: Compute the mass matrix $\mathbf{M}_a$ through (23)
3: Compute initial accelerations $\ddot{\mathbf{U}}_{t=0}$
4: **for** each time increment Δt **do**
5:     **Initialize:** $d\mathbf{U}_{n+1}^0 = \mathbf{0}$, $\mathbf{r}_{n+1-\alpha_f}^0 = \mathbf{r}_n$
6:     **for** $j = 0, 1, 2, \cdots$ **do**
7:         Compute tangential stiffness $\mathbf{K}_T^j$ through (41)
8:         Compute $\mathbf{K}_*^j$ through (40)
9:         Compute $\mathbf{G}(\mathbf{U}_{n+1}^j)$ through (37)
10:        Solve for $\Delta\mathbf{U}_{n+1}^{j+1}$ through (39)
11:        Update displacement increments $d\mathbf{U}_{n+1}^{j+1} = d\mathbf{U}_{n+1}^j + \Delta\mathbf{U}_{n+1}^{j+1}$
12:        Update displacements $\mathbf{U}_{n+1}^{j+1} = \mathbf{U}_{n+1}^j + d\mathbf{U}_{n+1}^{j+1}$
13:        Compute updated algorithmic internal force $\mathbf{r}_{n+1-\alpha_f}^{j+1}$ through (34) and (24)
14:        Compute accelerations $\ddot{\mathbf{U}}_{n+1}^{j+1}$ through (28)
15:        Compute residual $\mathbf{G}(\mathbf{U}_{n+1}^{j+1})$ through (37)
16:        **if** $\|\mathbf{G}(\mathbf{U}_{n+1}^{j+1})\| \leq tolerance$ **then** go to Step 20
17:        **else** go to Step 5
18:        **end if**
19:     **end for**
20:     Update velocities $\dot{\mathbf{U}}_{n+1}$ through (29)
21:     Update displacements $\mathbf{U}_{n+1} = \mathbf{U}_n + d\mathbf{U}_{n+1}$
22: **end for**

---

4. ENFORCEMENT OF ESSENTIAL BOUNDARY CONDITIONS

Due to the non-interpolatory properties of NURBS, essential boundary conditions in isogeometric analysis are generally enforced in a weak sense e.g. via a penalty approach [29], the Lagrange multiplier method [44] or Nitsche's method [81], etc. For special cases, where the model has simple geometries, a strong enforcement of the essential boundary conditions is also feasible. In the following, we first present the details of the weak enforcement of the essential boundary conditions in 4.1 and then followed by a detailed treatments of non-homogeneous displacement controlled essential boundary conditions in 4.2.

4.1. Weak enforcement of essential boundary conditions

The essential boundary conditions of the isogeometric Kirchhoff-Love shell are expressed in terms of midsurface displacements $\mathbf{u}$ and rotations $\mathbf{\Phi}_{(t)}$, respectively:

$$\mathbf{u} - \mathbf{u}_0 = \mathbf{0} \qquad \mathbf{x} \in \Gamma_u, \qquad (42)$$

$$\mathbf{\Phi}_{(t)} - \mathbf{\Phi}_{(t)0} = \mathbf{0} \qquad \mathbf{x} \in \Gamma_\theta, \qquad (43)$$

where a subscript 0 denotes prescribed values, and where a subscript (t) represents the components along the tangent of the boundary Γ_θ. The domain boundaries Γ_u and Γ_θ denote the Dirichlet boundary of prescribed essential boundary conditions. The total domain boundary Γ follows by unification with the Neumann boundary Γ_t of prescribed natural boundary conditions such that $\Gamma = \Gamma_u \cup \Gamma_\theta \cup \Gamma_t$ and $(\Gamma_u \cup \Gamma_\theta) \cap \Gamma_t = \emptyset$.

The governing equation (17) is extended to a formulation that enforces the displacement and rotational essential boundary conditions in a weak sense according to a pure penalty approach:

$$\int_A \mathbf{P}_0 \cdot \delta\mathbf{u}\, dA + \int_{\Gamma_t} \mathbf{T}_0 \cdot \delta\mathbf{u}\, d\Gamma \quad + \quad \int_{\Gamma_u} \delta\mathbf{T} \cdot (\mathbf{u}_0 - \mathbf{u})\, d\Gamma + \int_{\Gamma_\theta} \delta\mathbf{M}_{(t)} \cdot (\mathbf{\Phi}_{(t)0} - \mathbf{\Phi}_{(t)})\, d\Gamma$$

$$-\int_A (\mathbf{N} : \delta\varepsilon + \mathbf{M} : \delta\kappa)dA = \int_A \rho h \ddot{\mathbf{u}} \cdot \delta\mathbf{u}\, dA \tag{44}$$

where $\delta\mathbf{T}$ and $\delta\mathbf{M}_{(t)}$ are weight functions chosen to be $\delta\mathbf{T} = \epsilon\,\delta\mathbf{u}$ and $\delta\mathbf{M}_{(t)} = \epsilon\frac{h^2}{12}\delta\mathbf{\Phi}_{(t)}$, respectively, with ϵ representing a penalty factor. The values of penalty factor should not be too high and can be chosen in the range of Young's modulus as suggested in [29]. For homogeneous essential boundary conditions where $\mathbf{u}_0 = \mathbf{0}$, $\mathbf{\Phi}_{(t)0} = \mathbf{0}$, the governing equations (44) simplify to:

$$\int_A \mathbf{P}_0 \cdot \delta\mathbf{u}\, dA \;+\; \int_{\Gamma_t} \mathbf{T}_0 \cdot \delta\mathbf{u}\, d\Gamma - \int_{\Gamma_u} \epsilon\,\delta\mathbf{u} \cdot \mathbf{u}\, d\Gamma - \int_{\Gamma_\theta} \epsilon\frac{h^2}{12}\delta\mathbf{\Phi}_{(t)} \cdot \mathbf{\Phi}_{(t)}\, d\Gamma$$

$$-\int_A (\mathbf{N} : \delta\varepsilon + \mathbf{M} : \delta\kappa)dA = \int_A \rho h \ddot{\mathbf{u}} \cdot \delta\mathbf{u}\, dA\,. \tag{45}$$

The semi-discretized equilibrium equation reads:

$$\mathbf{f} - \mathbf{r} - \mathbf{r}_{(u)pen} - \mathbf{r}_{(\theta)pen} \quad = \quad \mathbf{M}_a\,\ddot{\mathbf{U}} \tag{46}$$

where

$$\mathbf{r}_{(u)pen} \quad = \quad \int_{\Gamma_u} \epsilon\,\mathbf{R}^T \cdot \mathbf{u}\, d\Gamma \tag{47}$$

$$\mathbf{r}_{(\theta)pen} \quad = \quad \int_{\Gamma_\theta} \epsilon\frac{h^2}{12}\frac{\partial\mathbf{\Phi}_{(t)}}{\partial\mathbf{U}} \cdot \mathbf{\Phi}_{(t)}\, d\Gamma \tag{48}$$

In terms of the generalized-α method, the effective structural equations of the shell including weak boundary conditions follow as:

$$\mathbf{r}(\mathbf{U}_{n+1-\alpha_f}) + \mathbf{r}_{(u)pen} + \mathbf{r}_{(\theta)pen} + \mathbf{M}_a\ddot{\mathbf{U}}_{n+1-\alpha_m} - \mathbf{f}_{n+1-\alpha_f} \quad = \quad \mathbf{G}_*(\mathbf{U}_{n+1}) \quad = \quad \mathbf{0} \tag{49}$$

which leads to the linearized form of the governing equation:

$$(\mathbf{K}_* + \mathbf{K}_{(u)pen} + \mathbf{K}_{(\theta)pen})\Delta\mathbf{U}_{n+1}^{k+1} \quad = \quad -\mathbf{G}_*(\mathbf{U}_{n+1}^k) \tag{50}$$

where

$$\mathbf{K}_{(u)pen} \quad = \quad \int_{\Gamma_u} \epsilon\,\mathbf{R}^T\mathbf{R}\, d\Gamma\,, \tag{51}$$

$$\mathbf{K}_{(\theta)pen} \quad = \quad \int_{\Gamma_\theta} \epsilon\frac{h^2}{12}\left[\frac{\partial\mathbf{\Phi}_{(t)}}{\partial\mathbf{U}}\right]^T \frac{\partial\mathbf{\Phi}_{(t)}}{\partial\mathbf{U}}\, d\Gamma + \int_{\Gamma_\theta} \epsilon\frac{h^2}{12}\frac{\partial^2\mathbf{\Phi}_{(t)}}{\partial\mathbf{U}\partial\mathbf{U}} \cdot \mathbf{\Phi}_{(t)}\, d\Gamma\,. \tag{52}$$

The rotation $\mathbf{\Phi}_{(t)}$ can be used to maintain clamped or symmetry boundary conditions along the shell's domain boundary [29]. The rotation and its variations are defined as:

$$\mathbf{\Phi}_{(t)} \quad = \quad \arcsin(\boldsymbol{\omega} \cdot \mathbf{t}) \tag{53}$$

$$\frac{\partial\mathbf{\Phi}_{(t)}}{\partial\mathbf{U}} \quad = \quad \frac{\boldsymbol{\omega}_{,\mathbf{U}} \cdot \mathbf{t}}{\sqrt{1 - (\boldsymbol{\omega} \cdot \mathbf{t})^2}} \tag{54}$$

$$\frac{\partial^2\mathbf{\Phi}_{(t)}}{\partial\mathbf{U}\partial\mathbf{U}} \quad = \quad \frac{\boldsymbol{\omega}_{,\mathbf{UU}} \cdot \mathbf{t}}{\sqrt{1 - (\boldsymbol{\omega} \cdot \mathbf{t})^2}} + \frac{(\boldsymbol{\omega}_{,\mathbf{U}} \cdot \mathbf{t})(\boldsymbol{\omega} \cdot \mathbf{t})(\boldsymbol{\omega}_{,\mathbf{U}} \cdot \mathbf{t})}{(1 - (\boldsymbol{\omega} \cdot \mathbf{t})^2)^{3/2}} \tag{55}$$

where the vector $\mathbf{t}$ is the unit tangent vector along the boundary Γ_θ, and where

$$\boldsymbol{\omega} \quad = \quad \mathbf{A}_3 \times (\mathbf{a}_3 - \mathbf{A}_3)\,, \tag{56}$$

$$\boldsymbol{\omega}_{,\mathbf{U}} \quad = \quad \frac{\partial \boldsymbol{\omega}}{\partial \mathbf{U}} = \mathbf{A}_3 \times \mathbf{a}_{3,\mathbf{U}}, \tag{57}$$

$$\boldsymbol{\omega}_{,\mathbf{UU}} \quad = \quad \frac{\partial^2 \boldsymbol{\omega}}{\partial \mathbf{U} \partial \mathbf{U}} = \mathbf{A}_3 \times \mathbf{a}_{3,\mathbf{UU}}. \tag{58}$$

The linearized form of the governing equation (50) is solved iteratively by a Newton-Raphson method.

4.2. An extention to non-homogeneous (displacement controlled) essential boundary conditions

For non-homogeneous essential boundary conditions, where $\mathbf{u}_0 \neq \mathbf{0}$ and $\boldsymbol{\Phi}_{(t)0} \neq \mathbf{0}$, modifications to the solution procedures in 4.1 are required. In this paper, we mainly focus on displacement controlled boundary conditions $\mathbf{u}_0 \neq \mathbf{0}$. Nevertheless, an extension to the situation of $\boldsymbol{\Phi}_{(t)0} \neq \mathbf{0}$ is straightforward.

4.2.1. Weak enforcement Considering $\mathbf{u}_0 \neq \mathbf{0}$, equation (44) can be formulated as:

$$\int_A \mathbf{P}_0 \cdot \delta\mathbf{u}\, dA \quad + \quad \int_{\Gamma_t} \mathbf{T}_0 \cdot \delta\mathbf{u}\, d\Gamma + \int_{\Gamma_u} \epsilon\, \delta\mathbf{u} \cdot \mathbf{u}_0\, d\Gamma - \int_{\Gamma_u} \epsilon\, \delta\mathbf{u} \cdot \mathbf{u}\, d\Gamma$$

$$- \int_A (\mathbf{N} : \delta\varepsilon + \mathbf{M} : \delta\kappa) dA = \int_A \rho h \ddot{\mathbf{u}} \cdot \delta\mathbf{u}\, dA \tag{59}$$

where, accordingly, the semi-discretized equilibrium equation can be rewritten as:

$$\mathbf{f} + \mathbf{f}_{(u)pen} - \mathbf{r} - \mathbf{r}_{(u)pen} \quad = \quad \mathbf{M}_a\, \ddot{\mathbf{U}} \tag{60}$$

in which the penalty contributions to the external forces $\mathbf{f}_{(u)pen}$ reads:

$$\mathbf{f}_{(u)pen} \quad = \quad \int_{\Gamma_u} \epsilon\, \mathbf{R}^T \cdot \mathbf{u}_0\, d\Gamma. \tag{61}$$

The effective structural equations of the shell can be rewritten as:

$$\mathbf{r}(\mathbf{U}_{n+1-\alpha_f}) + \mathbf{r}_{(u)pen} + \mathbf{M}_a \ddot{\mathbf{U}}_{n+1-\alpha_m} - \mathbf{f}_{n+1-\alpha_f} - \mathbf{f}_{(u)pen} \quad = \quad \mathbf{G}_*(\mathbf{U}_{n+1}) \quad = \quad \mathbf{0} \tag{62}$$

Similar to (38) and (50), the consistent linearization of (62) results in:

$$(\mathbf{K}_* + \mathbf{K}_{(u)pen})\Delta\mathbf{U}_{n+1}^{k+1} \quad = \quad -\mathbf{G}_*(\mathbf{U}_{n+1}^k) \tag{63}$$

which can be further rearranged as:

$$\begin{bmatrix} \mathbf{K}_*^{(11)} + \mathbf{K}_{(u)pen}^{(11)} & \mathbf{K}_*^{(12)} \\ \mathbf{K}_*^{(21)} & \mathbf{K}_*^{(22)} \end{bmatrix} \begin{bmatrix} \Delta\mathbf{U}_{n+1}^{(1),k+1} \\ \Delta\mathbf{U}_{n+1}^{(2),k+1} \end{bmatrix} \quad = \quad - \begin{bmatrix} \mathbf{G}_*^{(1)}(\mathbf{U}_{n+1}^k) \\ \mathbf{G}^{(2)}(\mathbf{U}_{n+1}^k) \end{bmatrix} \tag{64}$$

where superscript (1) represents the degrees-of-freedom associated to the displacement controlled boundary Γ_u, where superscript (2) represents the rest of the degrees-of-freedom, where $\Delta\mathbf{U}_{n+1}^{(i),k+1} = \mathbf{U}_{n+1}^{(i),k+1} - \mathbf{U}_{n+1}^{(i),k}$, $i \in \{1, 2\}$, and where $\mathbf{K}_{(u)pen}^{(11)}$ is the penalty stiffness matrix defined in (51) which contributes only at the first iteration ($k = 0$) of each load step.

For the first iteration of each load step, the residual $\mathbf{G}_*^{(1)}(\mathbf{U}_{n+1}^0)$ is:

$$\mathbf{G}_*^{(1)}(\mathbf{U}_{n+1}^0) \quad = \quad \mathbf{r}_{(u)pen}^{(1)} - \mathbf{f}_{(u)pen}^{(1)} \quad = \quad -\int_{\Gamma_u} \epsilon\, \mathbf{R}^{(1)T} \cdot \Delta\mathbf{u}_{n+1}\, d\Gamma \tag{65}$$

where $\Delta\mathbf{u}_{n+1} = (\mathbf{u}_0 - \mathbf{u})_{n+1} \in \mathbb{R}^3$ is the displacement increment of the Dirichlet boundary at the current load step, and where we assume that the equilibrium is satisfied at the end of the previous step n.

After solving (64) for the first iteration, the increments $\Delta\mathbf{U}_{n+1}^{(1),1}$ and $\Delta\mathbf{U}_{n+1}^{(2),1}$ are obtained. Then the first estimate of the algorithmic external forces is computed as:

$$
\begin{aligned}
\mathbf{f}_{n+1-\alpha_f}^{(1),1} &= \mathbf{K}_*^{(11)}\Delta\mathbf{U}_{n+1}^{(1),1} + \mathbf{K}_*^{(12)}\Delta\mathbf{U}_{n+1}^{(2),1} + \mathbf{r}_{n+1-\alpha_f}^{(1),0} \\
&\quad + \mathbf{M}_a^{(11)}\ddot{\mathbf{U}}_{n+1-\alpha_m}^{(1),0} + \mathbf{M}_a^{(12)}\ddot{\mathbf{U}}_{n+1-\alpha_m}^{(2),0}.
\end{aligned}
\tag{66}
$$

For subsequent iterations $(k \geq 1)$, the displacement increment $\Delta\mathbf{U}_{n+1}^{(1),k+1}$ is set to be zero, only $\Delta\mathbf{U}_{n+1}^{(2),k+1}$ is updated. Besides, the penalty terms in (62) are not required any more, since the displacement boundary conditions are already satisfied in the first iteration. Therefore, the linearized equation (64) reduces to:

$$
\begin{bmatrix} \mathbf{K}_*^{(11)} & \mathbf{K}_*^{(12)} \\ \mathbf{K}_*^{(21)} & \mathbf{K}_*^{(22)} \end{bmatrix} \begin{bmatrix} \mathbf{0} \\ \Delta\mathbf{U}_{n+1}^{(2),k+1} \end{bmatrix} = -\begin{bmatrix} \mathbf{G}^{(1)}(\mathbf{U}_{n+1}^k) \\ \mathbf{G}^{(2)}(\mathbf{U}_{n+1}^k) \end{bmatrix}
\tag{67}
$$

where

$$
\mathbf{G}^{(2)} = \mathbf{r}_{n+1-\alpha_f}^{(2),k} + \mathbf{M}_a^{(21)}\ddot{\mathbf{U}}_{n+1-\alpha_m}^{(1),k} + \mathbf{M}_a^{(22)}\ddot{\mathbf{U}}_{n+1-\alpha_m}^{(2),k}.
\tag{68}
$$

Substitution of (68) into (67) determines the increment $\Delta\mathbf{U}_{n+1}^{(2),k+1}$ which is used to update the external force:

$$
\mathbf{f}_{n+1-\alpha_f}^{(1),k+1} = \mathbf{K}_*^{(12)}\Delta\mathbf{U}_{n+1}^{(2),k+1} + \mathbf{r}_{n+1-\alpha_f}^{(1),k} + \mathbf{M}_a^{(11)}\ddot{\mathbf{U}}_{n+1-\alpha_m}^{(1),k} + \mathbf{M}_a^{(12)}\ddot{\mathbf{U}}_{n+1-\alpha_m}^{(2),k}.
\tag{69}
$$

Based on the above solution procedure, the nonlinear dynamic equations subjected to non-homogeneous (displacement controlled) essential boundary conditions can be solved effectively.

4.2.2. Strong enforcement as a special case For special cases, such as straight boundaries, non-homogeneous (displacement controlled) essential boundary conditions can be enforced in a strong sense on basis of prescribed displacement degrees-of-freedom at the boundary matching control points. The basic idea is similar to the weak approach, where the linearized governing equation is rearranged as:

$$
\begin{bmatrix} \mathbf{K}_*^{(11)} & \mathbf{K}_*^{(12)} \\ \mathbf{K}_*^{(21)} & \mathbf{K}_*^{(22)} \end{bmatrix} \begin{bmatrix} \Delta\mathbf{U}_{n+1}^{(1),k+1} \\ \Delta\mathbf{U}_{n+1}^{(2),k+1} \end{bmatrix} = -\begin{bmatrix} \mathbf{G}^{(1)}(\mathbf{U}_{n+1}^k) \\ \mathbf{G}^{(2)}(\mathbf{U}_{n+1}^k) \end{bmatrix}
\tag{70}
$$

Given the displacement increments $\Delta\mathbf{U}_{n+1}^{(1),1}$ for the first iteration of each time step, we have for the second row of (70):

$$
\Delta\mathbf{U}_{n+1}^{(2),1} = \left(\mathbf{K}_*^{(22)}\right)^{-1}\left(-\mathbf{G}^{(2)}(\mathbf{U}_{n+1}^0) - \mathbf{K}_*^{(21)}\Delta\mathbf{U}_{n+1}^{(1),1}\right) = \left(\mathbf{K}_*^{(22)}\right)^{-1}\left(-\mathbf{K}_*^{(21)}\Delta\mathbf{U}_{n+1}^{(1),1}\right)
\tag{71}
$$

where $\mathbf{G}^{(2)}(\mathbf{U}_{n+1}^0) = \mathbf{0}$ for the first iteration.

Based on the solution of $\Delta\mathbf{U}_{n+1}^{(2),1}$, the total displacement and accelerations of the shell are updated and the first estimation of the external force can be computed according to (66). For subsequent iterations, the iterative procedure is similar to Eqs. (67)-(69).

5. LEAST-SQUARES SURFACE FITTING OF GEOMETRIC IMPERFECTIONS

In this section, the least-squares fitting of the imperfect shell surfaces based on tensor-product B-spline surfaces is briefly described. Two error measures are presented which are used to evaluate the fitting quality.

The least-squares surface fitting problem can be stated as follows: Given a set of point data $\{\mathbf{C}_k\}_{k=1}^N$ in $\mathbb{R}^3$, we need to find corresponding parametric coordinates $\{(\xi_1, \xi_2)_k\}_{k=1}^N$ in $[0,1]^2$ and control points $\{\mathbf{P}_i\}_{i=1}^n$ of the B-spline surface $\bar{\mathbf{X}}$ such that the following least-squares sum is minimized

$$\sum_{k=1}^N \|\bar{\mathbf{X}}((\xi_1, \xi_2)_k) - \mathbf{C}_k\|^2 + \lambda \mathcal{R}(\mathbf{P}) \tag{72}$$

where $\bar{\mathbf{X}}$ is defined in (18), $\mathcal{R}(\mathbf{P})$ is a regularization term, herein chosen as:

$$\mathcal{R}(\mathbf{P}) = \iint_{[0,1]^2} (\|\bar{\mathbf{X}}_{\xi_1\xi_1}\|^2 + 2\|\bar{\mathbf{X}}_{\xi_1\xi_2}\|^2 + \|\bar{\mathbf{X}}_{\xi_2\xi_2}\|^2) d\xi_1 d\xi_2, \tag{73}$$

and λ is the non-negative weight used to balance the fitting error and the smoothness of the resulting surface. In our computations, we set $\lambda = 10^{-6}$.

Suppose that the knot vectors and orders of the B-spline surface are predefined, then the parametric coordinates $(\xi_1, \xi_2)_k \in [0,1]^2$ with respect to each point data $\mathbf{C}_k$ can be obtained by well established methods, such as Floater's parameterization method [82] etc. Consequently, the control points of the B-spline surface can be obtained by minimizing the least-squares sum (72), which leads to the following linear equations:

$$\mathbf{Q}\,\mathbf{P} \;=\; \mathbf{q} \tag{74}$$

where the matrix $\mathbf{Q}$ and vector $\mathbf{q}$ have the form:

$$\begin{aligned}
\mathbf{Q} \;&=\; \sum_{k=1}^N \mathbf{R}^T((\xi_1, \xi_2)_k)\mathbf{R}((\xi_1, \xi_2)_k) \\
&+ \lambda \iint_{[0,1]^2} \left(\frac{\partial^2 \mathbf{R}}{\partial \xi_1^2}\frac{\partial^2 \mathbf{R}^T}{\partial \xi_1^2} + 2\frac{\partial^2 \mathbf{R}}{\partial \xi_1 \partial \xi_2}\frac{\partial^2 \mathbf{R}^T}{\partial \xi_1 \partial \xi_2} + \frac{\partial^2 \mathbf{R}}{\partial \xi_2^2}\frac{\partial^2 \mathbf{R}^T}{\partial \xi_2^2} \right) d\xi_1 d\xi_2\,, \\
\mathbf{q} \;&=\; \sum_{k=1}^N \mathbf{R}^T((\xi_1, \xi_2)_k)\mathbf{C}_k\,.
\end{aligned} \tag{75}$$

We note that the regularization term ensures the unique solution of the least-squares fitting problem, since the first part of the equation (75) can be singular if a certain basis function vanishes on all the data points (i.e., no data points locate in its support). At the same time, this terms also ensures the smoothness of the resulting surface.

In order to evaluate the fitting quality of the resulting surface, we use a mean squared error measure (MSE) defined by

$$\text{MSE} \;=\; \frac{1}{N}\sum_{k=1}^N \|\bar{\mathbf{X}}((\xi_1, \xi_2)_k) - \mathbf{C}_k\|^2 \tag{76}$$

and a maximum error measure (ME) given by

$$\text{ME} \;=\; \max_{k \in \{1, 2, \ldots, n\}} \|\bar{\mathbf{X}}((\xi_1, \xi_2)_k) - \mathbf{C}_k\|. \tag{77}$$

Both error measures are considered in the following to ensure a highest level of accuracy.

6. NUMERICAL EXAMPLES

In this section, we test the efficiency and accuracy of the proposed method with several numerical examples including tumbling cylinder, cylindrical panel, conical shell and cylindrical

shell structures. The influence of numerical dissipation and the order of the approximation basis on the dynamic responses of shell structures are studied systematically. Besides, both man-made and measured geometric imperfections are introduced and their effects on the dynamic shell response is studied. For the dynamic analyses, the following adaptive time step size was used:

$$\Delta t = (I_0/I_n)\Delta t_p, \ I_n < I_{max} \tag{78}$$

where Δt_p and I_n are the time step size and number of iterations of the last time step, respectively, where I_0 and I_{max} are the desired and the maximum allowed number of iterations, respectively. If $I_n \geq I_{max}$, the current time step was re-computed with step size $\Delta t_p/2$. Alternatively, an adaptive time step size as proposed in [64] may also be used:

$$\Delta t = \begin{cases} \left(2 - \left(\frac{I_n-1}{I_0-1}\right)^2\right)\Delta t_p, \ I_n < I_0 \\ \left(1 - \frac{1}{2}\left(\frac{I_n-I_0}{I_{max}-I_0}\right)^2\right)\Delta t_p, \ I_n \geq I_0 . \end{cases} \tag{79}$$

We note that the adaptive time step size of (79) was adopted in sections 6.1-6.3, and the adaptive time step size of (78) was adopted in sections 6.4-6.5. The penalty factor ϵ in (45) and (59) was chosen in the following examples as $\epsilon = 100E$, where E is Young's modulus.
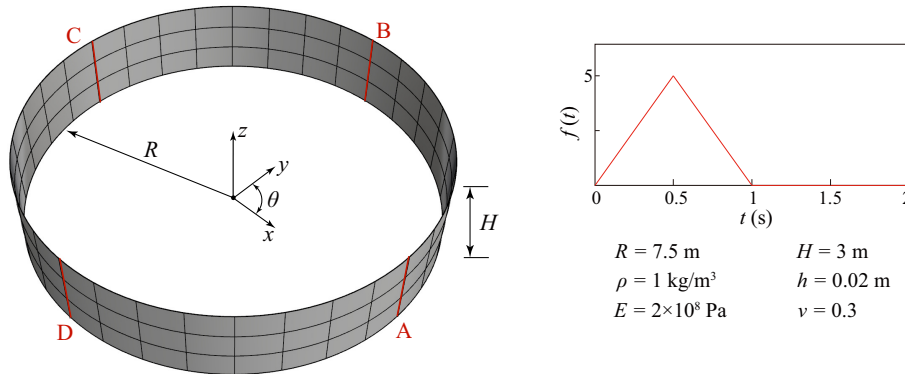
Figure 2. Tumbling cylinder: geometry, material properties and time histories of line loading.

6.1. Tumbling cylinder

In this example, the dynamic behavior of a tumbling cylinder [73] is studied to test the numerical stability and energy conservation properties of the proposed method. The geometric descriptions and material properties of the cylinder are shown in Figure 2, where no kinematic boundary conditions are enforced. The cylinder is discretized with 32×3 elements with $p_1 = p_2 = 3$. For the time step size control, we set $I_0 = 8$ and $I_{max} = 15$. Besides, we set an upper and lower bound for the time step size which is $\Delta t_{p_{max}} = 10^{-2}$s and $\Delta t_{p_{min}} = 10^{-4}$s. The cylinder was subjected to four line loads at the line segments A, B, C and D. These line forces are expressed as:

$$\mathbf{F}_A = \frac{4}{3}[0,-1,-1]^T f(t), \quad \text{at } \theta = 0$$

$$\mathbf{F}_B = \frac{4}{3}[1,1,1]^T f(t), \quad \text{at } \theta = \pi/2$$

$$\mathbf{F}_C = \frac{4}{3}[1,1,1]^T f(t), \quad \text{at } \theta = \pi$$

$$\mathbf{F}_D = \frac{4}{3}[0,-1,-1]^T f(t), \quad \text{at } \theta = 3\pi/2$$

where $f(t)$ is the loading function defined as:

$$f(t) = \begin{cases} 10t & \text{if } t \leq 0.5 \\ 5 - 10(t - 0.5) & \text{if } 0.5 < t \leq 1 \\ 0 & \text{if } t > 1 \end{cases}$$

Figure 3 shows the time history of energy for the tumbling cylinder problem, where the spectral radius was set to $\rho_\infty = 0.92$. It was found that the modified generalized-α method predicted almost constant energy even with a slight numerical dissipation. Higher values of ρ_∞ lead to numerical stability problems, possibly due to the introduced high frequency modes of the cubic NURBS basis functions. Figure 4 illustrates the tumbling of the cylinder, with the progressions of the deformed configurations shown sequentially from left to right.
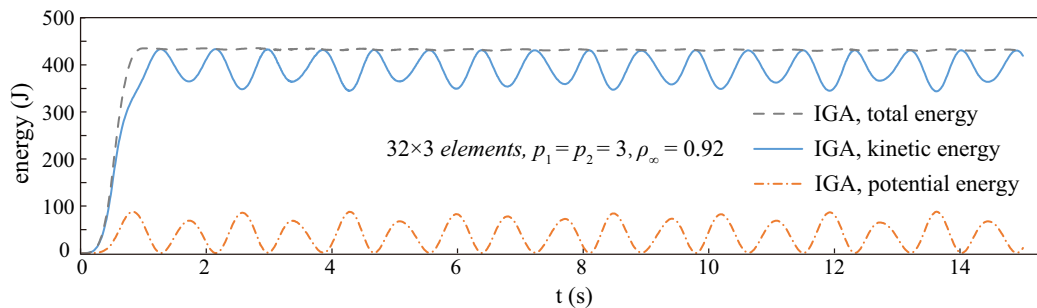
Figure 3. Tumbling cylinder: changes of energy.

Figure 4. Tumbling cylinder: sequence of deformed configurations.
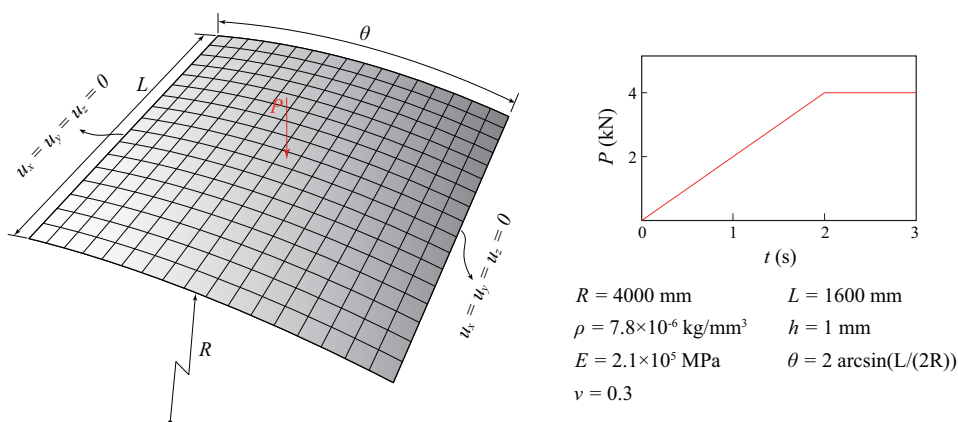
Figure 5. Thin cylindrical panel: geometry, boundary conditions, material properties and time histories of point loading.

6.2. Snap-through of thin cylindrical panel

In the second example, the snap-through of a thin cylindrical panel subjected to a centrally located point load P is studied. This simple model was chosen to test the implemented advancements on their reliability and to study the effect of numerical dissipation on the overall solution stability and solution quality. The geometry and material properties of the cylindrical panel as well as the time histories of P are shown in Figure 5. The cylindrical panel was fixed at the two straight boundaries and free at the circular boundaries. Different values of ρ_∞ in the generalized-α time integration method were chosen to study its high-frequency damping effects. Moreover, the influence of different mesh sizes and orders of the approximation basis were considered to obtain an optimal model configuration. For the time step size control, we set $I_0 = 8$ and $I_{max} = 15$. Besides, we set a upper and lower bound for the time step size which are $\Delta t_{p_{max}} = 10^{-2}$s and $\Delta t_{p_{min}} = 10^{-6}$s.

Figures 6-8 show the convergence properties of the cylindrical panel with a square, cubic, and quartic base, respectively, with the spectral radius set to $\rho_\infty = 0.7$. The panels with quadratic basis show stronger oscillations and slower convergence compared to their cubic and quartic counterparts. This behavior relativizes as the discretization becomes more refined, suggesting the use of more elements for $p_1 = p_2 = 2$. For the quartic-based panel, even a mesh with 9×9 elements was sufficient to obtain a convergent solution. It should be mentioned that the dynamic responses of the shell was slightly different at the snap-through stage, mainly due to the different meshes used (cf. Figures 7-8). Nevertheless, the pre-buckling and post-buckling responses of the shell showed excellent convergence properties for cubic and quartic basis.
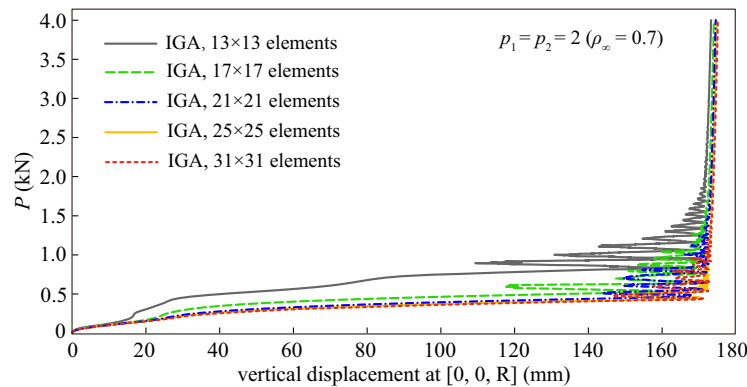

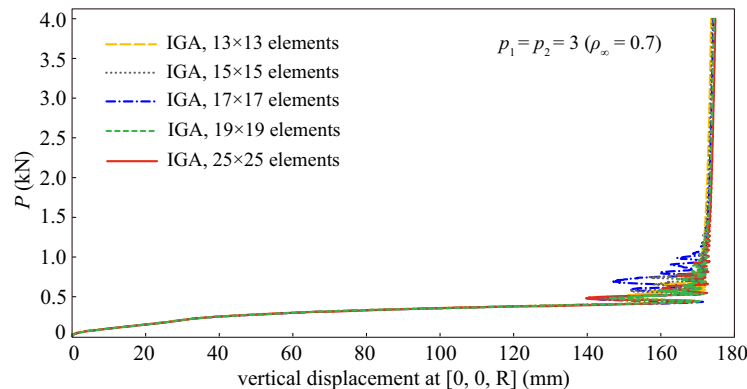Figure 6. Thin panel: convergence study with orders $p_1 = p_2 = 2$.

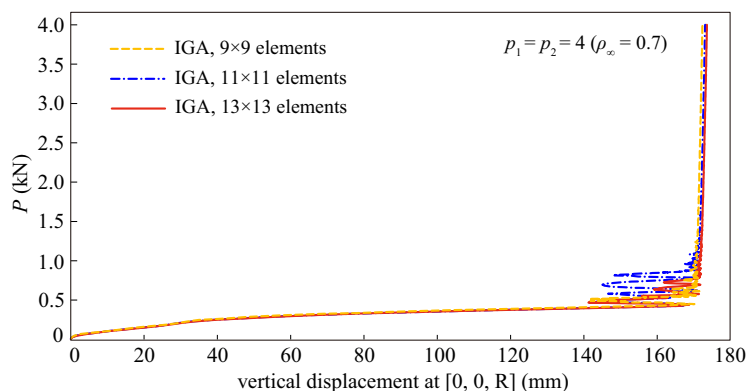Figure 7. Thin panel: convergence study with orders $p_1 = p_2 = 3$.

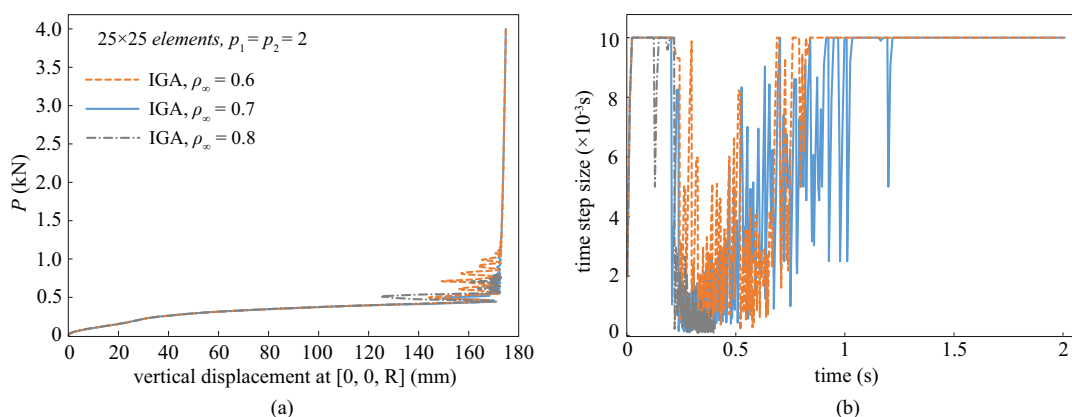Figure 8. Thin panel: convergence study with orders $p_1 = p_2 = 4$.

(a)   (b)

Figure 9. Thin panel ($p_1 = p_2 = 2$): (a) comparison of dynamic responses with different ρ_∞. (b) comparison of time step sizes.

Figures 9(a) - 11(a) show the effects of the numerical dissipation on the dynamic response of the panel with $p_1, p_2 \in \{2, 3, 4\}$. It can be seen that stable results were obtained with $\rho_\infty = 0.6$ and 0.7, while for $\rho_\infty = 0.8$ the panel oscillated strongly, which became even more evident for $p_1 = p_2 = 4$. It is highlighted that for $\rho_\infty = 0.8$ the dynamic analysis of the thin panel fails due to very small time step sizes. The time histories of the step size is depicted in Figures 9(b) - 11(b). The required step size for $\rho_\infty = 0.8$ was extremely small compared to the cases of $\rho_\infty = 0.6$ and 0.7. Moreover, the increase in numerical dissipation (decrease in ρ_∞) had a larger effect on the time step size of the quartic model suggesting that a higher artificial dissipation level is required when higher order basis functions are used.

In Figure 12(a), the dynamic responses of the IGA shell are compared with the reference FEM results [64] obtained with generalized-α method. It was found that the reference solution showed much higher oscillations than the IGA results and predicted slightly lower displacements after snap through. Besides, Figure 12(b) reconfirmed the need for a higher artificial dissipation when using higher order approximation to counteract the decreasing step size.

In Figure 13 is a comparison showing the difference in the dynamic responses of the shell when using the algorithmic internal force (33) and (34). The shell was discretized with 17×17 cubic elements, and the spectral radius was set to $\rho_\infty = 0.7$. It was found that the model with algorithmic internal force (33) fails to predict the correct snap-through behavior, which highlights the importance of choosing appropriate algorithmic internal forces.
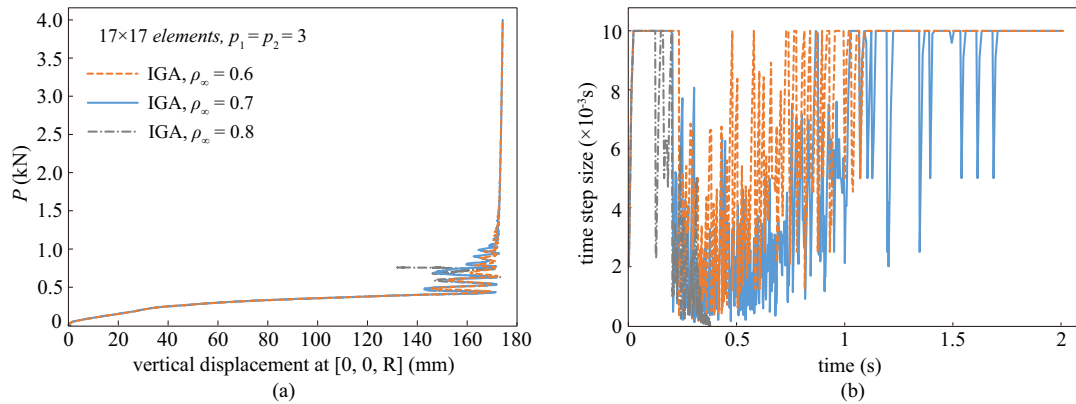
Figure 10. Thin panel ($p_1 = p_2 = 3$): (a) comparison of dynamic responses with different ρ_∞. (b) comparison of time step sizes.
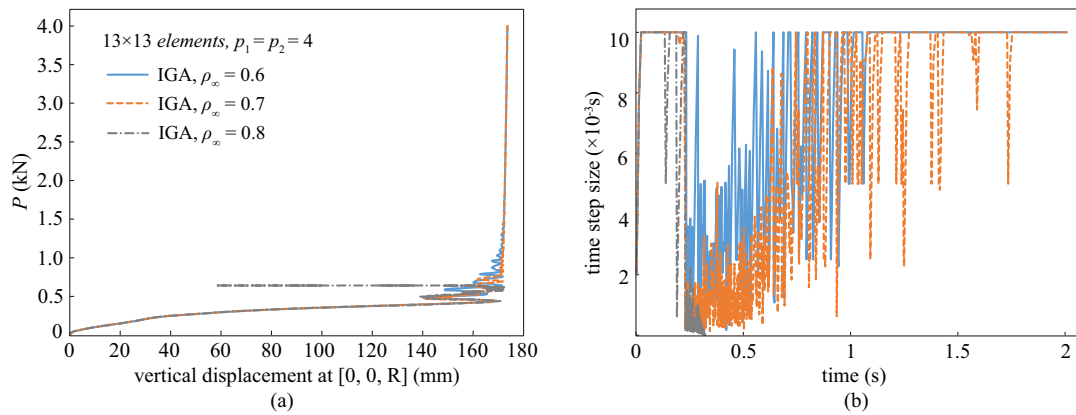

Figure 11. Thin panel ($p_1 = p_2 = 4$): (a) comparison of dynamic responses with different ρ_∞. (b) comparison of time step sizes.
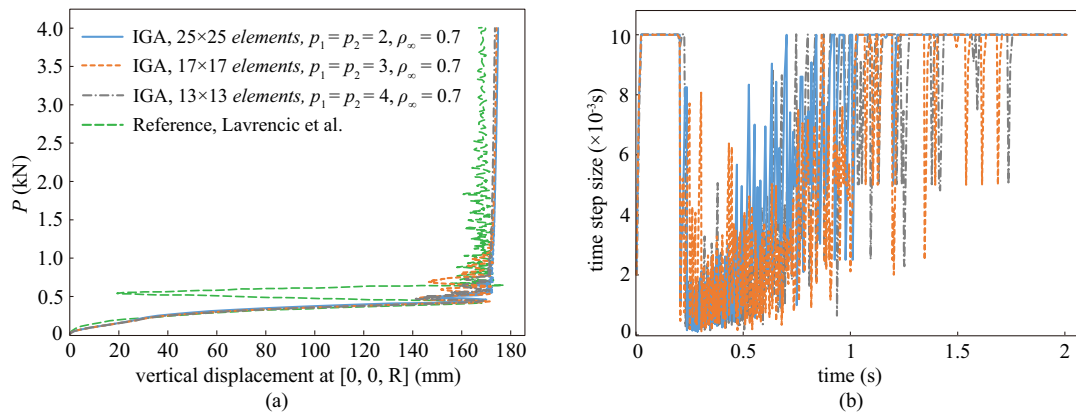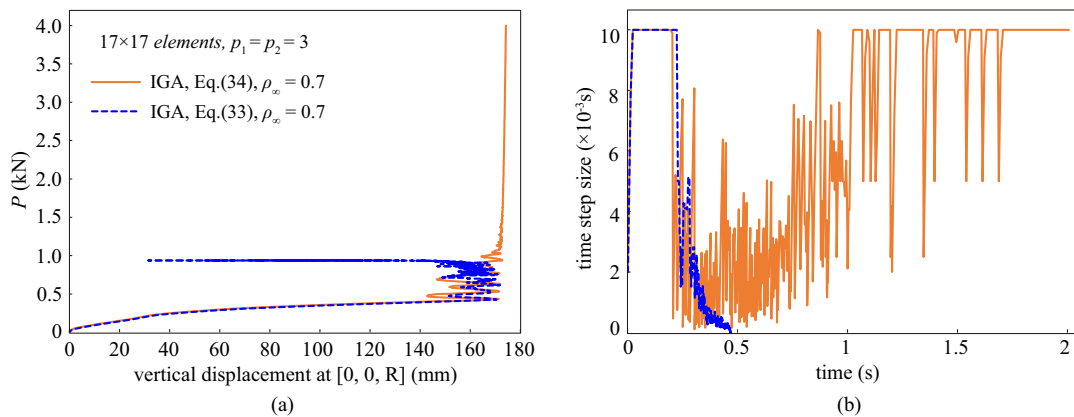

Figure 12. Thin panel: (a) comparison of IGA Kirchhoff-Love shell and FEM reference solutions. (b) comparison of time step sizes.

6.3. Snap-through of a conical shell

With the third example, the snap-through response of a conical shell was studied to confirm the influence of the fundamental modeling factors and numerical dissipation. The geometric description,

Figure 13. Thin panel ($p_1 = p_2 = 3$) : (a) comparison of dynamic responses with different algorithmic internal force. (b) comparison of time step sizes.

boundary conditions and material properties are depicted in Figure 14. Two load cases were considered in this example where the top edge was subjected (a) to an imposed displacement and (b) to an imposed line force, both in $-z$ direction. The time history for both load cases is shown in Figure 14. The desired and maximum allowed number of iterations for this example are $I_0 = 8$ and $I_{max} = 15$. Besides, the upper and lower bound of the time step size for the two load cases are: (a) $\Delta t_{p_{max}} = 2 \times 10^{-3}$s, $\Delta t_{p_{min}} = 10^{-5}$s and (b) $\Delta t_{p_{max}} = 10^{-2}$s, $\Delta t_{p_{min}} = 10^{-5}$s.
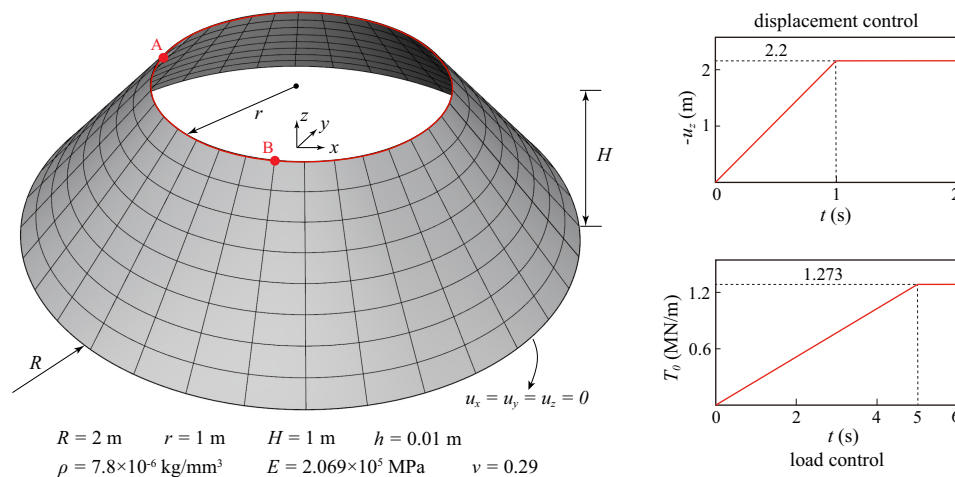

Figure 14. Conical shell: geometry, boundary conditions, material properties and time history of external loading

For the case of a line force loading, we used 48×15 elements with $p_1 = p_2 = 3$, while for $p_1 = p_2 = 2$, a discretization of 60×20 elements was adopted. Figures 15(a) - 16(a) show the load-displacement responses of the conical shell using a quadratic and a cubic basis, respectively, considering different values of ρ_∞. For a comparison of the results, the dynamic responses at the locations $A = [-r, 0, H]$ and $B = [0, -r, H]$ were selected.

The conical shell, which uses a quadratic approximation basis, buckled at a load level of 1.55×10^6N - slightly larger than in the cubic case with a buckling load of 1.48×10^6 N. Besides, Figures 15(b) - 16(b) show the time step sizes of the conical shell during snap-through. For both values, $\rho_\infty = 0.6$ and $\rho_\infty = 0.7$, the shell which used a cubic approximation basis led to smaller time step sizes than for the quadratic case. In Figure 17 contour plots of the conical shell at various time steps are shown. The buckling initiates at the upper rim of the conical shell and propagates through the
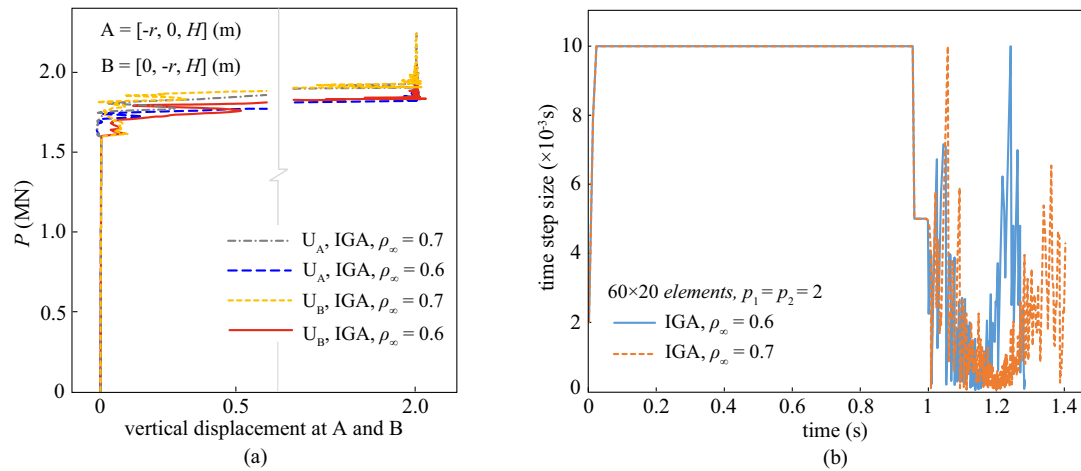
Figure 15. Conical shell under line load ($p_1 = p_2 = 2$): (a) dynamic response of point A and B with $\rho_\infty = 0.6$ and 0.7. (b) comparisons of time step sizes.
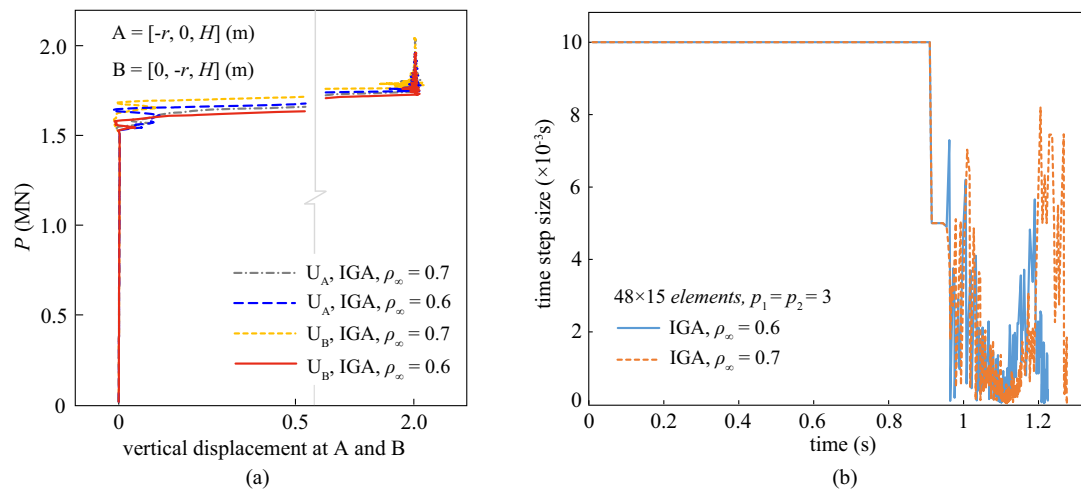

Figure 16. Conical shell under line load ($p_1 = p_2 = 3$): (a) dynamic response of point A and B with $\rho_\infty = 0.6$ and 0.7. (b) comparisons of time step sizes.

whole structure. The snap-through phenomenon was initiated around the time $t = 1.083$ s and ended around the time $t = 1.100$ s, when a completely reversed configuration was reached. For animations of the complete response, we refer the reader to [83].

For the load case of imposed displacements, two mesh configurations of 48×15 and 60×20 were considered using a quadratic approximation basis. In addition, a cubic approximation basis with 48×15 elements, similar to the line load case, was adopted. Figures 18(a) and 19(a) show the dynamic responses of the shell upper edge for the quadratic and cubic case, respectively. It can be observed from Figure 19(a) that, the shell with cubic basis was able to capture the initial buckling load with a coarse mesh of 48×15 elements. While for the quadratic basis, a much finer mesh of 60×20 elements was required. The buckling loads predicted by our IGA model and a reference FEM model using 80×20 elements is listed in Table I and reveal good agreement with the FEM solutions. For the cubic IGA model, the buckling load is slightly lower compared to the reference solutions obtained from dynamic and static arc-length solutions. Remarkable in this comparison is the point of time when buckling occurs. The IGA model buckles after almost half the time found for the FEM model which can be traced back to larger time steps, especially at the beginning of the analysis, cf. Figure 18(b) and Figure 19(b). In addition, it should be noted that the cubic shell
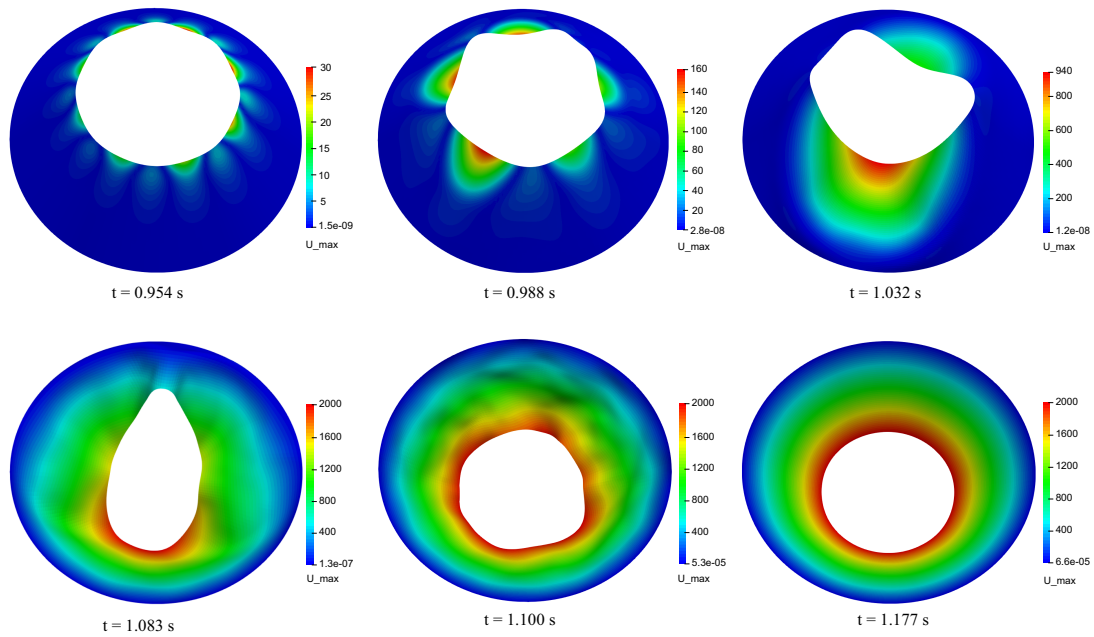
Figure 17. Contour plots of the conical shell at different time steps: line force, 48×15 elements, $p_1 = p_2 = 3$, $\rho_\infty = 0.6$.
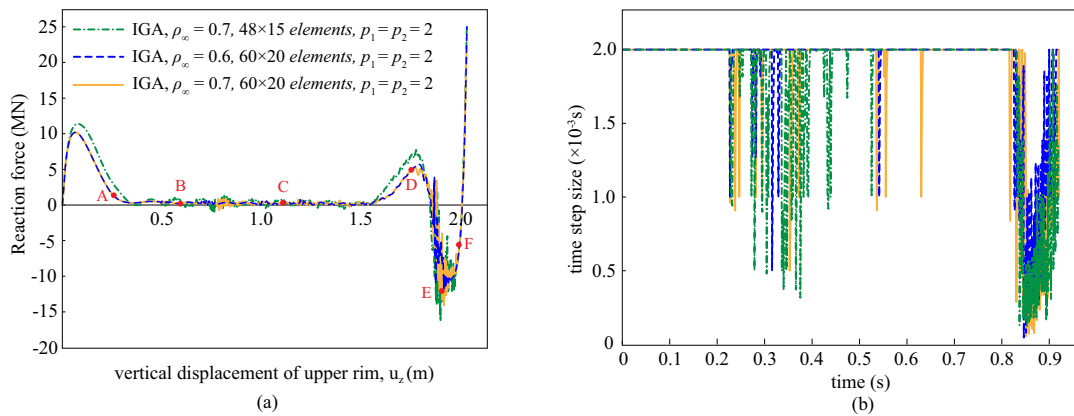

Figure 18. Conical shell under prescribed displacement ($p_1 = p_2 = 2$): (a) comparisons of dynamic responses with $\rho_\infty = 0.6$ and 0.7. (b) comparisons of time step sizes.

suffered from high frequency oscillations during the snap-through. This behavior became even more severe for $\rho_\infty = 0.7$, cf. Figure 20. In contrast, the quadratic shell showed less oscillations and in comparison exhibited relatively large time step sizes, cf. Figures 18(b), 19(b) and 20. Again a higher numerical dissipation was required for the higher order model to obtain an appropriate time step size.

Table I. Comparison of buckling loads for the load case of imposed displacements on the upper rim of the conical shell.

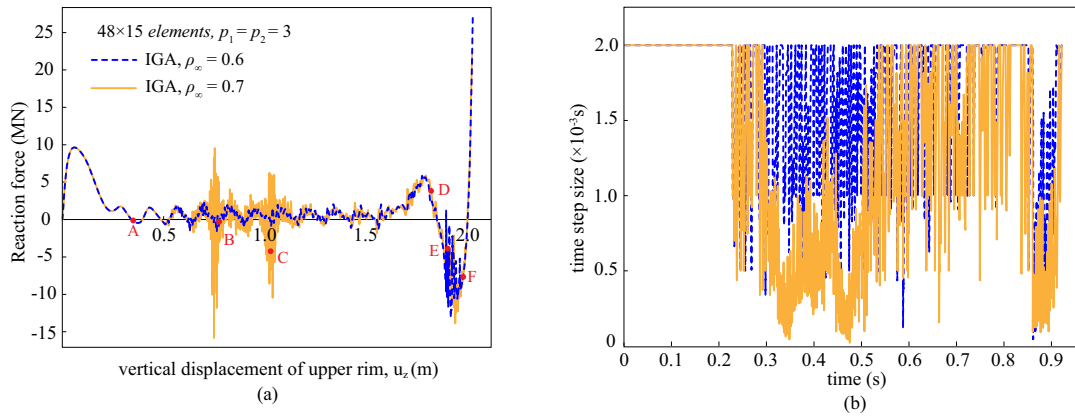| method	IGA		FEM [64]		
	p=2	p=3	Generalized-α	HHT-α	static arc-length
buckling load (kN)	10185	9640	10247	10021	9960
buckling time (s)	0.03	0.028	0.048	0.047	0.051

Figure 19. Conical shell under prescribed displacement ($p_1 = p_2 = 3$): (a) comparisons of dynamic responses with $\rho_\infty = 0.6$ and 0.7. (b) comparisons of time step sizes.
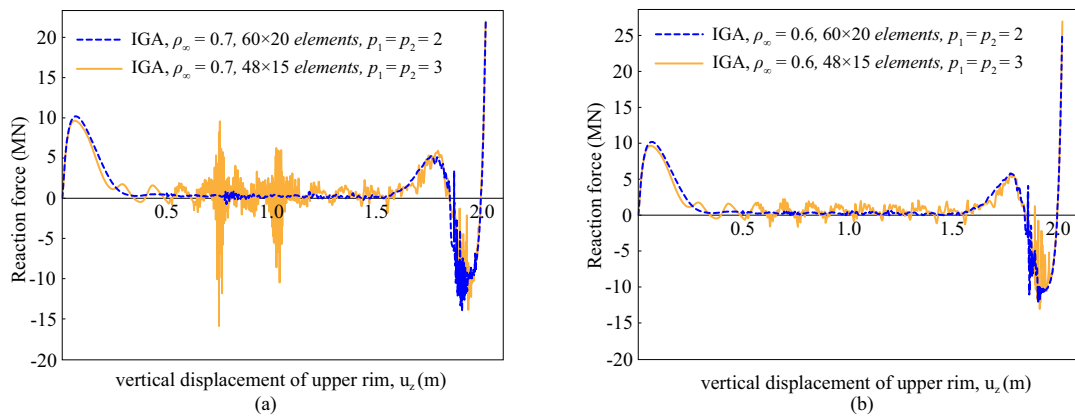

Figure 20. Conical shell under prescribed displacement: (a) comparisons of dynamic responses with $\rho_\infty = 0.7$. (b) comparisons of dynamic responses with $\rho_\infty = 0.6$.

In Figures 21 and 22 contour plots of the conical shell at different time steps for the quadratic and cubic model, respectively, are depicted. In contrast to the force line loading where the upper rim of the conical shell was allowed to move freely (cf. Figure 17), the prescribed displacement boundary conditions impose strong restrictions on the movement of the upper rim, hence, a local buckling phenomenon was frequently observed to release elastic energy during snap-through. In addition, the cubic model behaved somewhat softer and exhibited pronounced local buckling compared to the quadratic model, cf Figure 21 ($t = 0.504$ s) and Figure 22 ($t = 0.466$ s), respectively.

6.4. Buckling of axially loaded cylinder

With this example, we consider the dynamic buckling of a cylindrical shell. The geometry, material properties and boundary conditions as shown in Figure 23 were taken from [84]. This example originates from Yamaki's experiments [85], who manufactured these cylinders carefully with polyethylene terephthalate in order to remove geometric imperfections. The cylinder was subjected to an imposed displacement on its top circular edge which was increased linearly from 0 to 1 mm within a time span of 2 s. Both cylinders with perfect geometry and imposed imperfections were investigated. The spectral radius was set to be $\rho_\infty = 0.6$. In addition, the desired and maximum allowed number of iterations were set to be $I_0 = 8$ and $I_{max} = 15$. The theoretical critical buckling
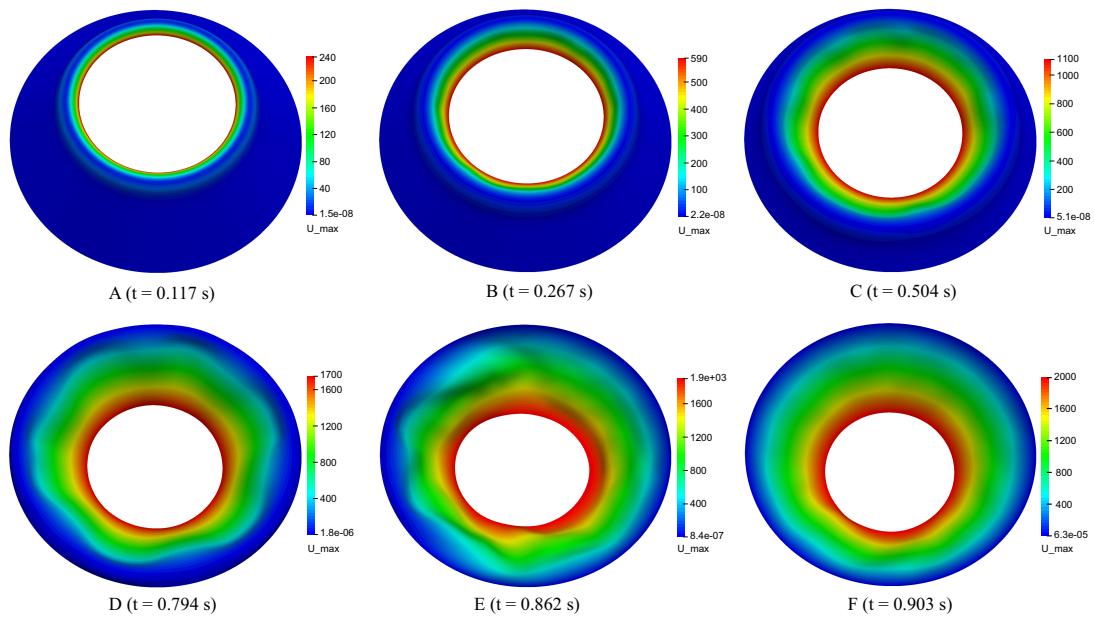
Figure 21. Contour plots of the conical shell at different time steps: imposed displacement, 60×20 elements, $p_1 = p_2 = 2$, $\rho_\infty = 0.7$.
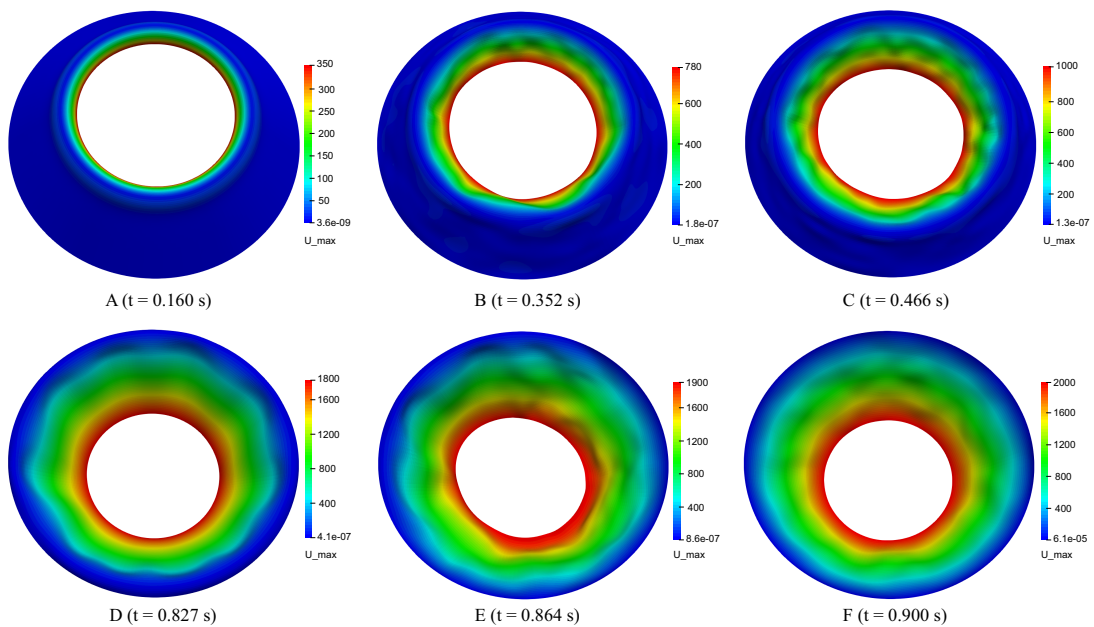

Figure 22. Contour plots of the conical shell at different time steps: imposed displacement, 48×15 elements, $p_1 = p_2 = 3$, $\rho_\infty = 0.7$.

load of the cylinder is 1289.9 N, which was found according to [86]:

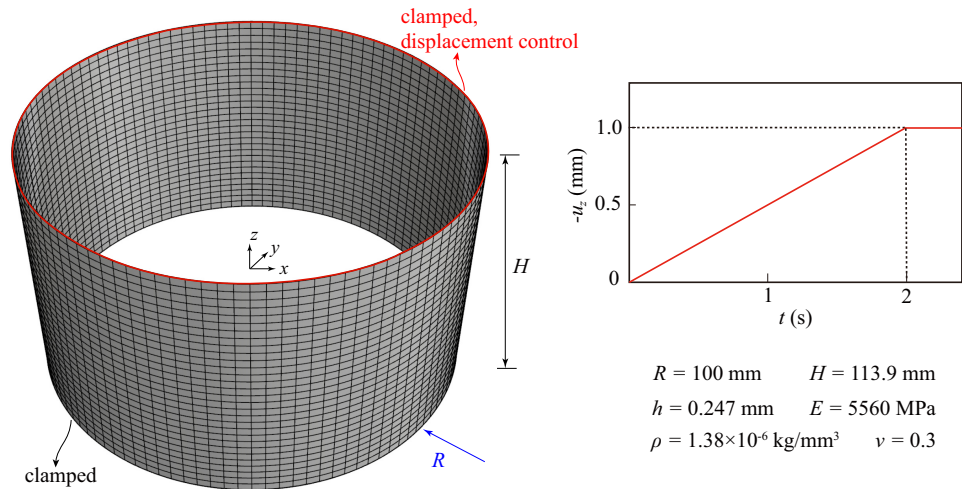$$P_{cr} = \frac{2\pi\, h^2 E}{\sqrt{3(1-\nu^2)}} \,. \tag{80}$$

Figure 23. Axially loaded cylinder: geometry, boundary conditions, material properties and time history of external loading.
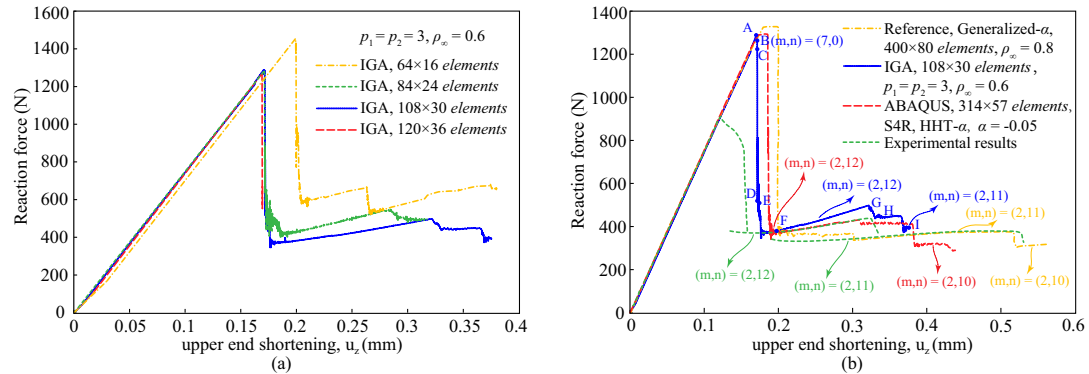

Figure 24. Axially loaded cylinder: (a) convergence of cubic IGA model with $\rho_\infty = 0.6$. (b) comparison of dynamic responses with reference solutions.

6.4.1. Cylinder without geometric imperfections For the perfect cylinder, a convergence study was performed for the IGA model and compared to reference FEM solutions [64], cf Figure 24. From Figure 24(a) it can be seen that the IGA solution converged to a buckling load of 1284.9 N with a mesh of 108×30 cubic elements. In Figure 24 (b) a comparison of the IGA results with reference solutions as well as experimental results are depicted.

The buckling loads of the different IGA models agree very well with solutions found with ABAQUS [87] in which 314×57 S4R elements were used. The ABAQUS solution shows a small plateau after the initial buckling load is reached, while the IGA model shows an immediate loss of load-carrying capacity, leading to a jump from an asymmetric mode to a rhombic mode (see configurations B-F in Figure 25). The FEM reference solution used 400×80 elements in combination with a generalized-α time integration scheme and resulted in a slightly higher buckling load and an even more pronounced plateau after the buckling load was reached.

The experimental buckling load of the cylinder was much lower than numerical predictions which is due to the inherent geometric imperfections of the manufactured cylinder. Nevertheless, this example shows that the IGA method can capture the theoretical buckling load with a much smaller number of elements compared to the FEM reference solutions, thanks to the geometric accuracy and the high order continuous basis.
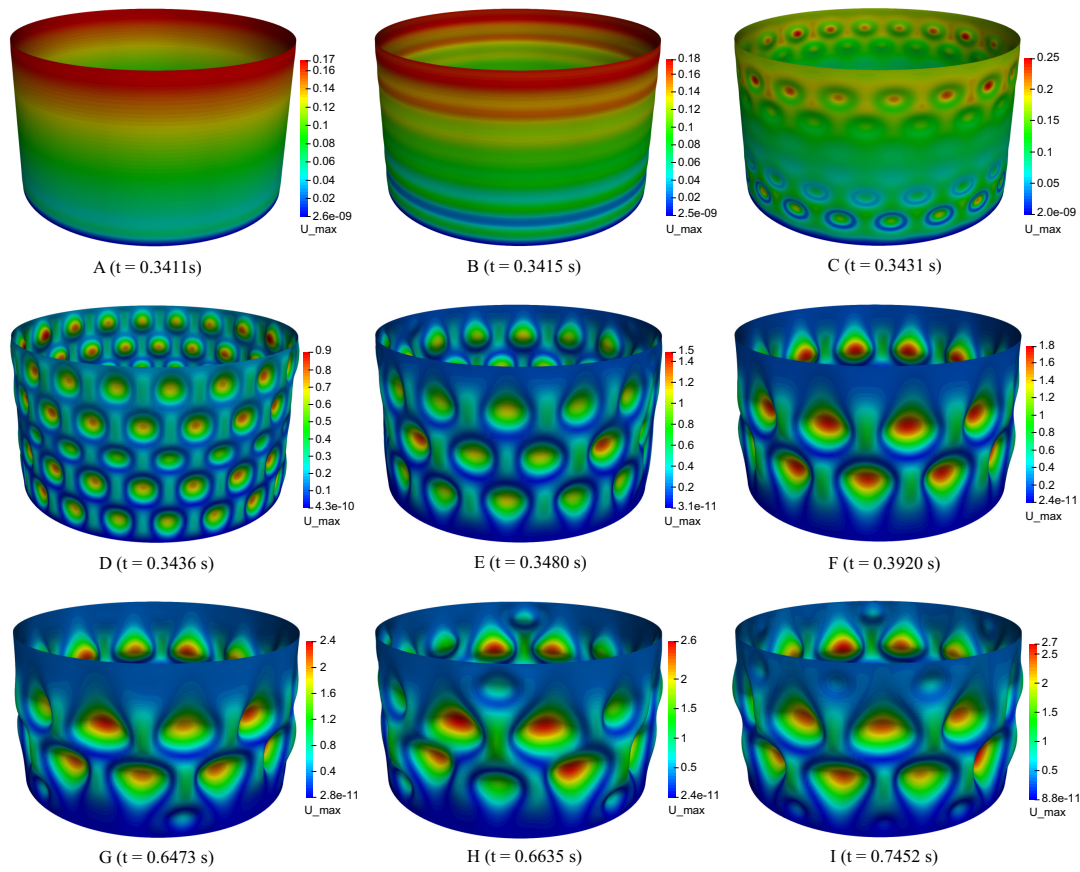
Figure 25. Contour plots of the axially loaded cylinder at different time steps: imposed displacement, 108×30 elements, $p_1 = p_2 = 3$, $\rho_\infty = 0.6$

In addition, the IGA model was able to capture the mode type $(m, n) = (2, 12)$ after the initial snap-through of the cylinder (see configuration F in Figure 25), where m and n denotes the number of half-waves in the axial direction and the number of full-waves in the circumferential direction, respectively. When the applied displacement increased, the IGA model jumped to a mode type of $(m, n) = (2, 11)$ (see configuration I in Figure 25) which agreed well with the experimental results, cf. Figure 24 (b). We note, that the ABAQUS model omitted the buckling mode of $(m, n) = (2, 11)$ and jumped directly to the mode of $(m, n) = (2, 10)$. The reference FEM model omitted the buckling mode of $(m, n) = (2, 12)$ and jumped to the mode of $(m, n) = (2, 11)$.

6.4.2. Cylinder with geometric imperfections In order to study the influence of geometric imperfections on the dynamic buckling behavior of the cylinder, various types of initial geometric imperfections can be introduced, such as single eigenmodes or a factorized sum of several eigenmodes. In [84], it is reported that, the first 18 eigenmodes of the cylinder can be described by the following half-wave and full wave numbers: $m = 13$ and $n = 0, \cdots, 7$, and $m = 12$ and $n = 0, \cdots, 9$. Following the approach of [64], the geometric imperfections can be described by the factorized sum of the first 18 eigenmodes which is represented by the following function:

$$\bar{w}(\theta, z) = \frac{h}{100} \left(\sum_{m=12}^{13} \sin\left(\frac{m\pi z}{H}\right) + \sum_{n=1}^{7} \sin(n\theta) \sin\left(\frac{13\pi z}{H}\right) + \sum_{n=1}^{9} \sin(n\theta) \sin\left(\frac{12\pi z}{H}\right) \right) \quad (81)$$

where z is the axial coordinate and θ denotes the circumferential angle, where the amplitude of the geometric imperfection is set to be $\frac{h}{100}$. The geometric imperfection $\bar{w}$, shown in Figure 26, is then added to the cylinder radius to generate a set of data points $\mathbf{C}_k$. Next, the IGA cylinder with
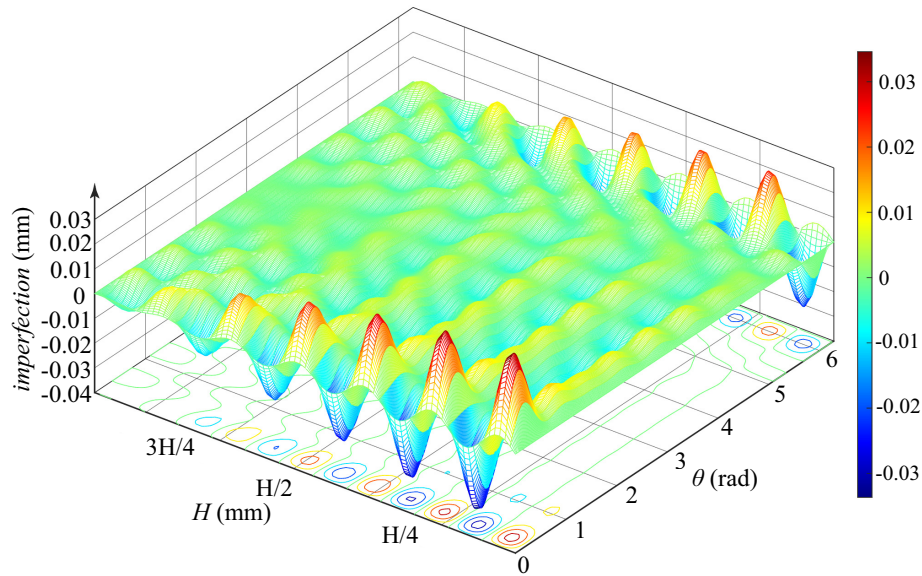
Figure 26. Buckling of axially loaded cylinder: contour plots of the geometric imperfections.

geometric imperfections is obtained through a least-squares surface fitting approach presented in section 5.
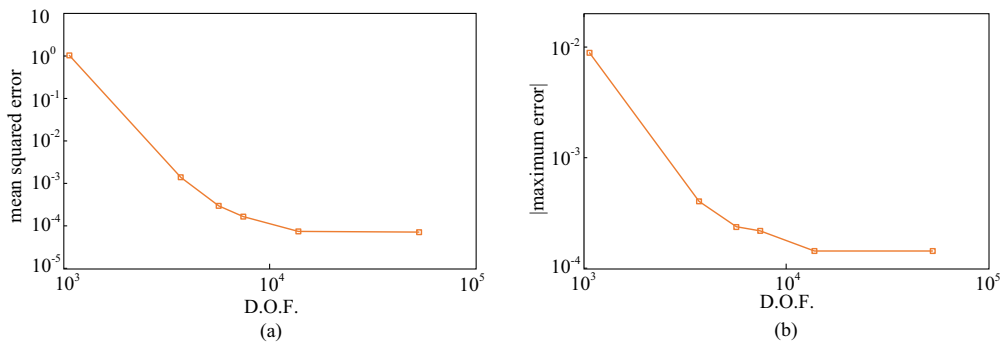

Figure 27. Convergence study of geometric imperfection modeling of cylinder: (a) square root of mean square error. (b) absolute value of maximum error.

A set of cubic B-spline surfaces with 50×16, 100×32, 120×42, 140×48, 200×64 and 400×128 elements were generated to represent the imperfection model. The convergence of the approximation error for the different meshes is shown in Figure 27 for the two error measures of section 5 revealing that a mesh of 120×42 elements (16605 DOF) is sufficiently accurate to represent the geometric imperfections given by (81). The contour plots of the approximation error using 120×42 elements is shown in Figure 28, where the following norm is adopted:

$$\epsilon \quad = \quad \frac{100 \, |\bar{\mathbf{X}} - \bar{\mathbf{X}}_{exact}|}{h} \tag{82}$$

where $\bar{\mathbf{X}}_{exact}$ is the target imperfection surface. It was found that, the maximum approximation error is around 0.1% of the shell thickness (10% of the imperfection amplitude), located at the position of the largest geometric imperfections.

In Figures 29 (a) and (b) the convergence studies of the imperfect cylindrical shell using IGA and ABAQUS, respectively, is depicted. The IGA model predicted the buckling load with a mesh of 120×42 elements, while for the ABAQUS model a converged buckling load was difficult to predict
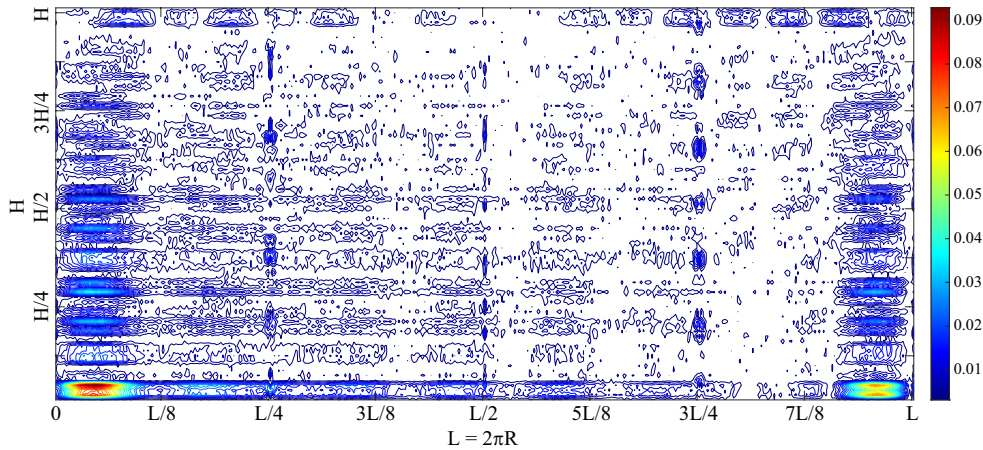
Figure 28. Axially loaded cylinder: contour plots of the surface fitting error with 120×42 elements.
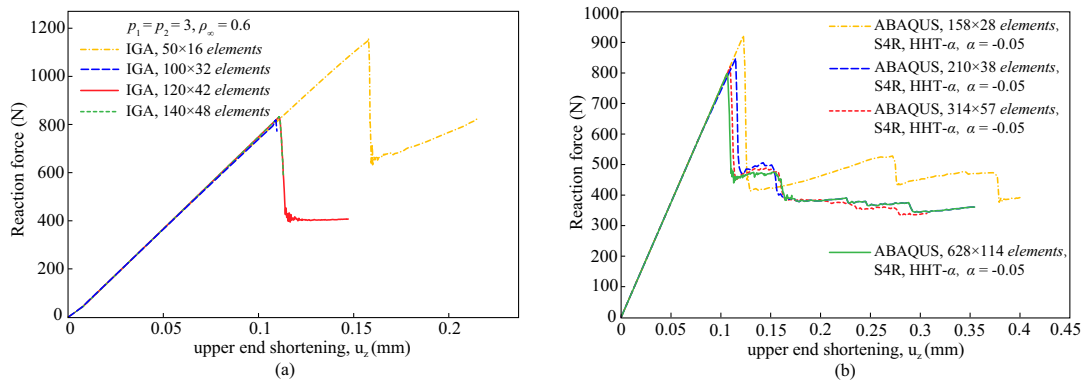

Figure 29. Axially loaded imperfect cylinder: (a) convergence of IGA method using cubic basis and $\rho_\infty = 0.6$. (b) convergence of ABAQUS method using HHT-α method.

unambiguously even with a fine mesh of 628×114 elements. This confirms the prominent role of geometric imperfection modeling in the analysis of shell buckling. The IGA model fully exploits the smooth and higher order continuous geometry representation which in contrast to the linear facet elements used in ABAQUS seems to be a decisive factor for the reliability of the analysis. We note, that with a mesh of 120×42 elements, both key factors, imperfection fitting and dynamic buckling load, were reliably and well predicted with the IGA model.

In Figure 30 a comparison of the dynamic response of the imperfect cylinder obtained with IGA, reference FEM solutions as well as experiments is illustrated. The buckling loads of each method were: (i) 830.7 N for IGA method, (ii) 820.2 N for ABAQUS, (iii) 890.3 N for the reference FEM model with generalized-α method, (iv) 808.3 N for the reference FEM model with Bossak method and (v) 911.2 N for the experiment. We note, that with geometric imperfections the buckling loads decreased dramatically compared to the perfect cylinder (cf. Figure 24 (b)), which signifies a key role of considering geometric imperfections in shell buckling. Compared to the experimental results, the IGA and FEM reference solutions were slightly lower (about 8%), which we attribute to the shape of the geometric imperfections introduced in (81).

In Figure 31 the contour plots of the imperfect cylinder during buckling is shown. It was observed that buckling started at the local dimple (see configuration B in Figure 31), then spreaded out in the circular direction (see configurations D-E in Figure 31) and finally arrived at a mode of $(m, n) = (2, 13)$ (see configuration F in Figure 31). We note that the slight deviation of the kink mode compared to the experiments could be due to the shape of the geometric imperfections introduced in (81). Nevertheless, the evolution of buckling modes predicted by IGA method agree
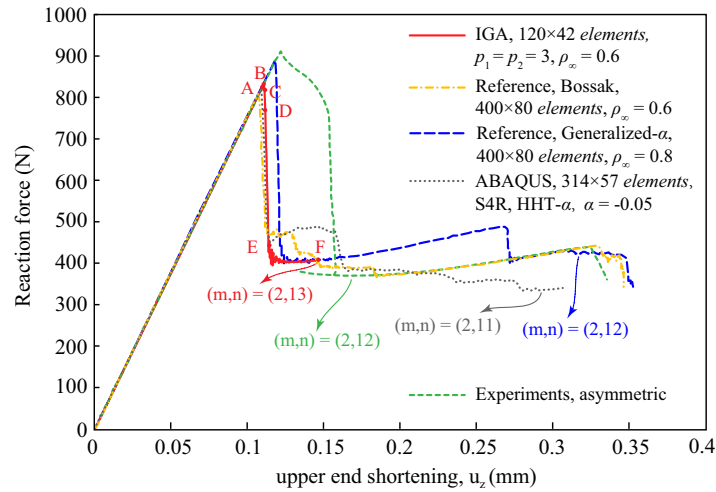
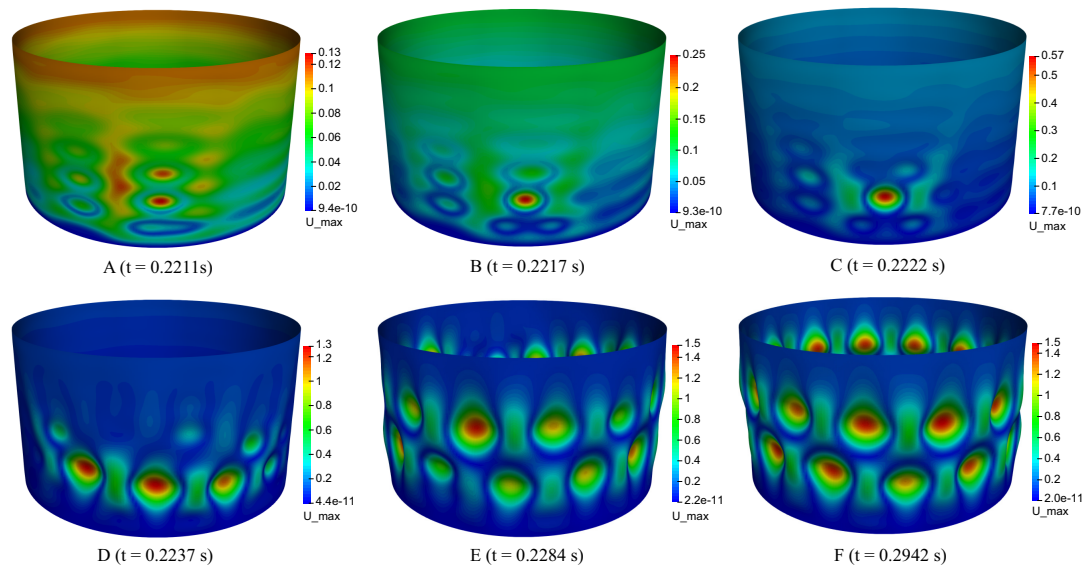Figure 30. Axially loaded imperfect cylinder: comparison of dynamic responses.

Figure 31. Contour plots of the axially loaded imperfect cylinder at different time steps: imposed displacement, 120×42 elements, $p_1 = p_2 = 3$, $\rho_\infty = 0.6$.

well with the reference FEM solutions (blue curve in Figure 30), in which the shell jumped to a buckling mode of $(m, n) = (2, 12)$ at $u_z = 0.27$ mm. The further buckling mode transition was exactly the same as for the perfect cylinder and experiment. In contrast, the ABAQUS solution shows a jump directly from the initial buckling mode to the mode of $(m, n) = (2, 11)$ (gray curve in Figure 30).

6.5. Buckling of cylinder with measured geometric imperfections

We close the example section with a cylinder under compression for which a measured imperfection model is available. The cylinder was subjected to a uniform imposed displacement along the upper rim, and clamped along both the upper and bottom rims. The loading rate of the upper rim was -0.5mm/s. The geometry of the model is similar to the previous example (cf. Figure 23), with $R = 101.6$ mm, $h = 0.1128$ mm and $H = 171.45$ mm. The material properties of the cylinder were: $E = 104110$ MPa, $\nu = 0.3$ and $\rho = 8.96 \times 10^{-6}$ kg/mm^3. In addition, the desired and maximum

allowed number of iterations were set to be $I_0 = 8$ and $I_{max} = 15$. Real geometric imperfection data for the cylinder was provided by the imperfection model data base of TU Delft, NL [88], from which measurements of a series of cylinders from a common manufacturing process were available. The cylinder, labeled A13, was taken exemplarily from [88]. The real imperfect geometry of the cylinder was provided in terms of the perfect structure and a series of two-dimensional Fourier coefficients to allow for a simple reconstruction of the imperfection data. The half-wave cosine representation of the geometric imperfections involved two sets of $m \times n$ harmonic components A_{kl} and B_{kl} according to the following Fourier representation:

$$\bar{w}(z, \theta,) = h \sum_{k=0}^{m} A_{k0} \cos\left(\frac{k\pi z}{H}\right) + h \sum_{k=0}^{m} \sum_{l=1}^{n} \cos\left(\frac{k\pi z}{H}\right) (A_{kl} \cos(l\theta) + B_{kl} \sin(l\theta)) \quad (83)$$

where the Fourier coefficients of the cylinder A13 are provided in the Table II of Appendix A. The measured imperfection field $\bar{w}$, shown in Figure 32, was added to the perfect cylinder to generate the real geometries of the cylindrical shell.
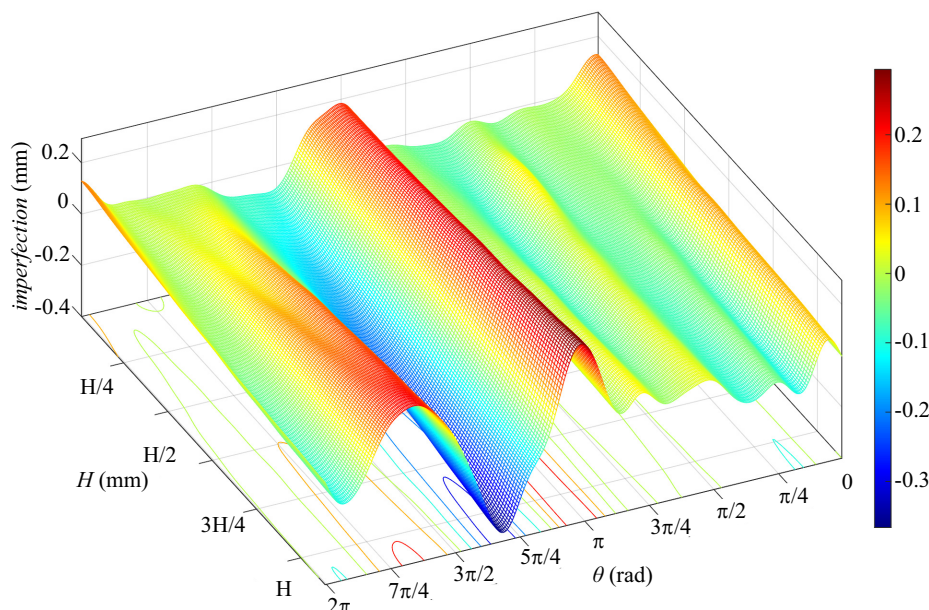

Figure 32. Cylinder with measured geometric imperfections: contour plots of the geometric imperfections.

A set of cubic B-spline surfaces with 60×16, 80×22, 100×27, 120×32, 140×38, 160×43 and 240×64 elements were generated to represent the imperfection model. The convergence of the approximation error for the different meshes is shown in Figure 33. A mesh of 140×38 elements provided a sufficiently accuracy to represent the geometric imperfections given by (83). The contour plots of the approximation error using 140×38 elements is shown in Figure 34, where the maximum approximation error is around 0.09% of the shell thickness. We note that the following norm is adopted in Figure 34:

$$\epsilon = \frac{|\bar{\mathbf{X}} - \bar{\mathbf{X}}_{exact}|}{h} \quad (84)$$

In Figure 35(a), the dynamic response of the isogeometric model using different numbers of elements is shown. A mesh of 140×38 elements was sufficient to predict the buckling load of the imperfect cylinder A13 at 4693 N. Figure 35(b) shows a comparison of the IGA and ABAQUS solutions, where 212×57 elements were used with ABAQUS. The buckling load predicted from the ABAQUS model was 4674 N, which fits well the IGA solution. Regarding the buckling modes,
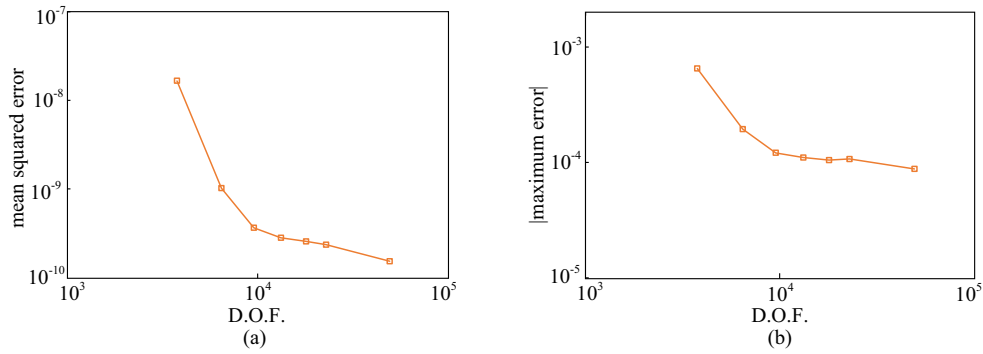
Figure 33. Convergence study of geometric imperfection modeling of cylinder A13: (a) square root of mean square error. (b) absolute value of maximum error.
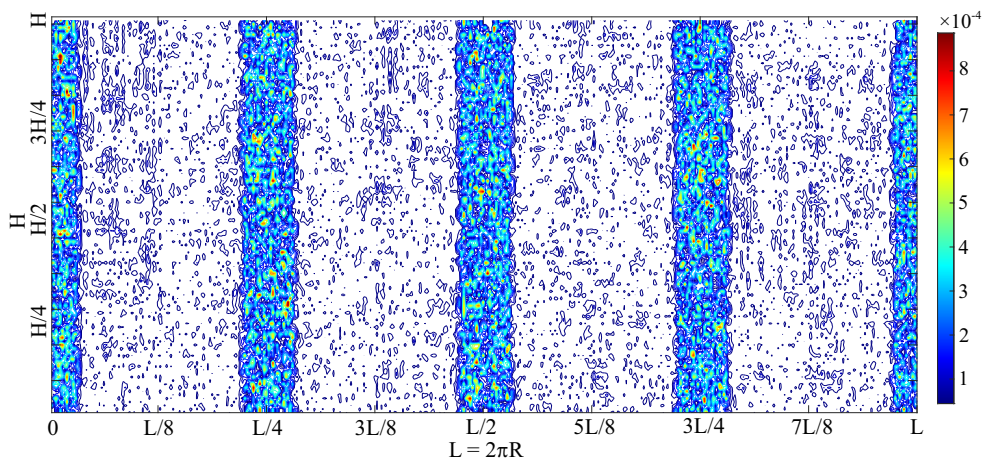
Figure 34. Cylinder with measured geometric imperfections: contour plots of the surface fitting error with 140×38 elements.
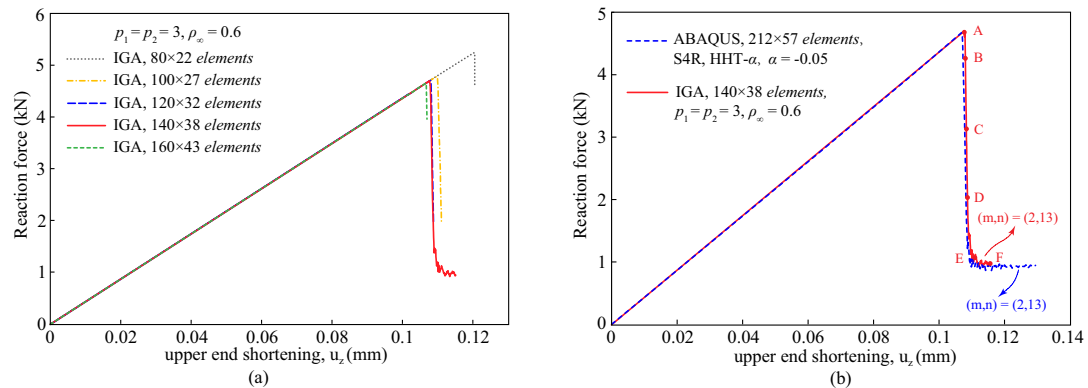
Figure 35. Cylinder with measured geometric imperfections: (a) convergence of IGA method using cubic basis and $\rho_\infty = 0.6$. (b) comparisons of IGA and ABAQUS methods.

the cylinder started to buckle near its upper rim where several local dimples are initiated (see configuration A in Figure 36). Then, the local buckling spreaded out in both circular and axial directions (see configurations B-C in Figure 36). Finally, small buckling modes merged with each other until a stable buckling mode $(m, n) = (2, 13)$ was reached (see configurations D-F in Figure
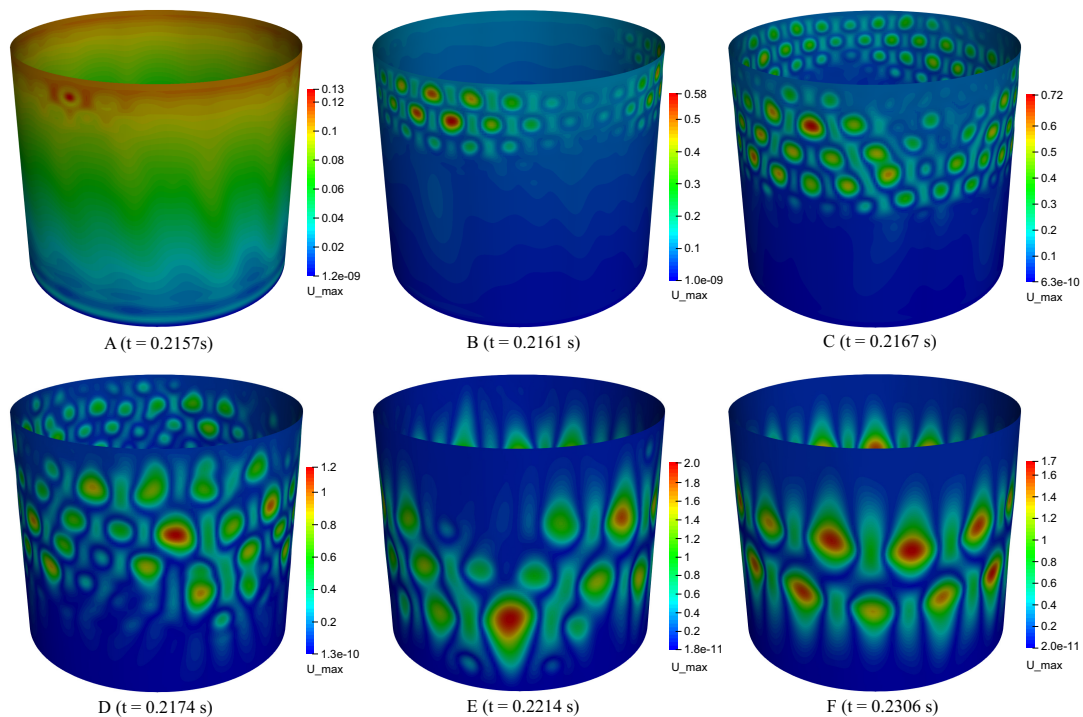
Figure 36. Contour plots of the cylinder A13 at different time steps: imposed displacement, 140×38 elements, $p_1 = p_2 = 3$, $\rho_\infty = 0.6$.

36). We note that both, the IGA and the ABAQUS model well predicted the stable buckling mode of $(m, n) = (2, 13)$.

7. SUMMARY AND CONCLUSIONS

In this paper, we proposed and tested a comprehensive framework for dynamic buckling analysis of shells based on isogeometric analysis. It includes a rotation-free Kirchhoff-Love shell element, a generalized-α time integration scheme with controllable numerical dissipation and applies an approach to enforce essential boundary conditions in a weak sense that allows unconstrained NURBS modeling. A least-squares surface fitting approach with corresponding error measures was introduced to take geometric imperfections into account. The imperfection model is based on B-spline surfaces to support the underlying isogeometric paradigm of seamlessly merging CAD modeling and numerical analysis and to profit from the overall smoothness properties of splines for an undisturbed geometric imperfection model.

We tested and assessed the performance of our analysis framework with a series of numerical examples that involve snap-through and collapse phenomena. We studied the energy conserving properties of the method using an example of a tumbling cylinder where a nearly constant energy is obtained with a small numerical dissipation. We investigated the modeling error for different discretizations for a thin curved panel and a conical shell structure, varying the number of elements and the order of the approximation basis. Numerical dissipation was assessed on basis of the time step size for different NURBS which confirmed the need for higher dissipation with increasing order of the approximation basis to damp properly the influence of higher frequencies. Compared with a classical FEM shell solution the IGA model was capable to remove significant parts of disturbing oscillations of the buckling load solution. In all computations a significantly larger time step size was possible compared to FEM reference models without compromising the reliability of the computation and solution quality. A penalty based weak enforcement approach for essential

boundary conditions was tested with a displacement-controlled buckling test for the conical shell structure which very well agreed for the predicted buckling load with FEM results from literature.

For an example of a perfect cylindrical shell, we demonstrated superior convergence properties of the IGA model in terms of initial buckling loads and buckling modes compared to FEM reference solutions. The IGA model well captured a mode jumping behavior that was in perfect agreement with the experimental results. Considering geometric imperfections, a B-spline-based least squares surface fitting could be applied directly in the dynamic buckling analysis loop. The generated imperfection model led to an accurate prediction of the buckling load and the corresponding mode shape. In contrast, the determination of the buckling load predicted by ABAQUS showed extreme mesh sensitivity, indicating a severe deficiency in the linear facet elements used to represent the ABAQUS imperfection model.

Finally, we demonstrated reliability and accuracy of the proposed framework using a cylinder with measured geometric imperfections. Both, buckling load and buckling modes were well captured with a significantly smaller number of elements compared to the ABAQUS reference solutions. Future research should focus on studying the dynamic behavior of shell structures with complex geometries where trimming and coupling of multiple patches is required.

A. MEASURED GEOMETRIC IMPERFECTION DATA

Table II. Fourier coefficients of the half-wave cosine representation of A13 shell [88].

A_{kl}

l =	0	1	2	3	4	5	6	7	8	9	10	11	12	13	14
k=0	0.002	0.0	0.469	-0.699	0.504	-0.040	0.097	0.031	0.189	-0.055	0.055	-0.010	-0.026	-0.031	-0.016
k=1	0.024	0.0	0.127	0.304	-0.053	0.046	-0.018	-0.006	-0.079	0.060	-0.036	0.020	0.059	-0.004	0.017
k=2	0.009	-0.009	-0.010	0.011	0.002	-0.008	0.012	0.0	0.013	0.011	-0.002	-0.012	0.023	0.033	-0.006
k=3	0.0	0.0	0.025	0.033	-0.018	0.008	0.013	0.002	-0.015	0.013	0.0	0.0	-0.009	0.005	0.008
k=4	0.005	-0.003	0.008	0.002	-0.009	0.001	0.013	-0.002	-0.003	0.005	0.005	-0.005	-0.001	0.004	0.0
k=5	-0.002	0.0	0.012	0.012	-0.009	0.003	0.006	-0.001	-0.007	0.005	0.001	0.0	-0.002	0.001	0.001
k=6	-0.005	-0.002	0.003	0.003	0.0	-0.004	0.004	0.004	-0.003	0.002	0.0	0.004	0.002	0.004	0.0
k=7	0.006	-0.002	0.0	0.008	0.002	-0.002	0.0	0.0	0.0	0.0	-0.002	0.0	-0.002	-0.002	0.002
k=8	0.004	0.0	-0.004	0.002	0.003	-0.001	0.0	0.0	0.002	0.001	0.0	-0.001	0.001	0.001	-0.001
k=9	-0.004	0.003	0.0	0.005	-0.001	0.001	0.0	0.0	0.0	0.001	0.0	0.0	0.0	0.0	0.001
k=10	0.0	-0.003	0.0	0.0	-0.002	0.0	0.0	-0.001	0.0	-0.002	-0.001	0.0	0.0	0.002	0.0
k=11	0.003	0.0	0.002	0.002	0.002	0.002	0.0	0.0	0.0	0.0	0.0	0.0	0.0	0.0	0.0
k=12	0.0	0.002	-0.003	0.001	0.0	0.0	0.0	0.0	0.001	0.0	0.0	0.0	0.0	0.0	0.0
k=13	-0.002	-0.002	0.0	0.0	0.0	0.0	0.001	0.002	0.0	0.0	-0.001	0.002	0.0	-0.001	0.001

B_{kl}

l =	0	1	2	3	4	5	6	7	8	9	10	11	12	13	14
k=0	0	0.0	-0.509	0.042	0.395	-0.018	0.141	-0.021	0.105	0.130	0.021	0.022	0.016	0.023	0.019
k=1	0	0.004	0.404	-0.094	-0.195	-0.002	-0.062	-0.049	-0.018	-0.025	-0.061	-0.024	-0.025	-0.004	-0.009
k=2	0	0.007	-0.002	-0.003	0.009	-0.018	0.002	0.016	-0.020	-0.014	0.004	0.007	-0.008	-0.003	-0.019
k=3	0	-0.012	0.045	-0.006	-0.021	-0.009	-0.004	0.002	-0.005	-0.003	-0.002	0.009	-0.003	0.007	0.0
k=4	0	-0.013	0.002	0.009	0.0	-0.015	0.002	0.013	-0.009	-0.007	0.004	0.007	-0.004	-0.001	0.0
k=5	0	-0.010	0.017	0.004	-0.008	-0.007	-0.004	0.005	0.0	-0.005	0.0	0.006	0.0	0.0	0.001
k=6	0	0.002	0.0	0.0	0.0	0.0	-0.001	0.001	0.0	-0.003	-0.002	0.0	0.0	-0.001	0.0
k=7	0	0.002	0.008	-0.003	-0.002	0.002	-0.002	-0.002	0.001	0.0	-0.001	0.001	0.0	0.001	0.002
k=8	0	0.005	0.0	-0.003	0.0	0.0	-0.002	0.0	0.0	0.001	0.0	0.002	0.0	0.0	-0.003
k=9	0	0.002	0.0	-0.002	-0.003	0.0	-0.001	0.0	-0.001	0.0	-0.001	0.0	0.0	0.0	0.0
k=10	0	-0.002	0.004	0.0	0.0	-0.002	0.002	0.0	-0.003	0.0	0.002	0.0	0.0	0.0	-0.002
k=11	0	0.0	0.0	-0.001	0.0	0.0	0.0	0.0	0.0	0.0	-0.002	0.0	0.001	0.002	0.0
k=12	0	0.0	0.0	-0.001	0.0	-0.001	0.0	0.0	-0.001	0.0	0.001	0.0	0.0	0.002	0.0
k=13	0	0.0	0.002	0.0	0.0	0.0	0.001	0.0	0.0	0.0	0.001	0.001	0.0	0.001	0.0

References

1. Simitses G. Buckling and postbuckling of imperfect cylindrical shells: A review. *Applied Mechanics Reviews* 1986; **39(10)**:1517–1524.
2. Arbocz J, Starnes Jr JH. Future directions and challenges in shell stability analysis. *Thin-Walled Structures* 2002; **40**:729–754.
3. Elishakoff I. Uncertain buckling: its past, present and future. *International Journal of Solids and Structures* 2000; **37(46-47)**:6869–6889.
4. Arbocz J, Babcock Jr CD. The effect of general imperfections on the buckling of cylindrical shells. *Journal of Applied Mechanics* 1969; **36(1)**:28–38.
5. Chryssanthopoulos MK, Poggi C. Probabilistic imperfection sensitivity analysis of axially compressed composite cylinders. *Engineering Structures* 1995; **17(6)**:398–406.
6. Schenk CA, Schuëller GI. Buckling analysis of cylindrical shells with random geometric imperfections. *International Journal of Non-Linear Mechanics* 2003; **38**:1119–1132.
7. Papadopoulos V, Papadrakakis M. The effect of material and thickness variability on the buckling load of shells with random initial imperfections. *Computer Methods in Applied Mechanics and Engineering* 2005; **194**:1405–1426.
8. Papadopoulos V, Stefanou G, Papadrakakis M. Buckling analysis of imperfect shells with stochastic non-gaussian material and thickness properties. *International Journal of Solids and Structures* 2009; **46**:2800–2808.
9. Degenhardt R, Kling A, Bethge A, Orf J, Kärger L, Zimmermann R, Rohwer K, Calvi A. Investigations on imperfection sensitivity and deduction of improved knock-down factors for unstiffened CFRP cylindrical shells. *Composite Structures* 2010; **92**:1939–1946.
10. Bisagni C. Composite cylindrical shells under static and dynamic axial loading: An experimental campaign. *Progress in Aerospace Sciences* 2015; **78**:107–115.
11. Koiter W. On the stability of the elastic equilibrium. PhD Thesis, Delft University of Technology 1945.
12. Budiansky B, Hutchinson W. A survey of some buckling problems. *AIAA Journal* 1966; **4**(9):1505–1510.
13. Stefanou G, Papadrakakis M. Stochastic finite element analysis of shells with combined random material and geometric properties. *Computer Methods in Applied Mechanics and Engineering* 2004; **193**:139–160.
14. Liang K, Ruess M, Abdalla M. The Koiter-Netwon approach using von Kármán kinematics for buckling analyses of imperfection sensitive structures. *Computer Methods in Applied Mechanics and Engineering* 2014; **279**:440–468.
15. Leonetti L, Magisano D, Liguori F, Garcea G. An isogeometric formulation of the koiter's theory for buckling and initial post-buckling analysis of composite shells. *Computer Methods in Applied Mechanics and Engineering* 2018; **337**:387–410.
16. Wang B, Ma X, Hao P, Sun Y, Tian K, Li G, Zhang K, Jiang L, Guo J. Improved knockdown factors for composite cylindrical shells with delamination and geometric imperfections. *Composite Part B: Engineering* 2019; **163**:314–323.
17. Hughes T, Cottrell J, Bazilevs Y. Isogeometric analysis: CAD, finite elements, NURBS, exact geometry and mesh refinement. *Computer Methods in Applied Mechanics and Engineering* 2005; **194**:4135–4195.
18. Kiendl J, Bletzinger KU, Linhard J, Wüchner R. Isogeometric shell analysis with Kirchhoff-Love elements. *Computer Methods in Applied Mechanics and Engineering* 2009; **198(49-52)**:3902–3914.
19. Benson D, Bazilevs Y, Hsu M, Hughes T. A large deformation, rotation-free, isogeometric shell. *Computer Methods in Applied Mechanics and Engineering* 2011; **200**:1367–1378.
20. Benson D, Bazilevs Y, Hsu M, Hughes T. Isogeometric shell analysis: the Reissner-Mindlin shell. *Computer Methods in Applied Mechanics and Engineering* 2010; **199**:276–289.
21. Dornisch W, Klinkel S, Simeon B. Isogeometric Reissner-Mindlin shell analysis with exactly calculated director vectors. *Computer Methods in Applied Mechanics and Engineering* 2013; **253**:491–504.
22. Echter R, Oesterle B, Bischoff M. A hierarchic family of isogeometric shell finite elements. *Computer Methods in Applied Mechanics and Engineering* 2013; **254**:170–180.
23. Hosseini S, Remmers J, Verhoosel C, Borst R. An isogeometric solid-like shell element for nonlinear analysis. *International Journal for Numerical Methods in Engineering* 2013; **95**:238–256.
24. Bouclier R, Elguedj T, Combescure A. An isogeometric locking-free NURBS-based solid-shell element for geometrically nonlinear analysis. *International Journal for Numerical Methods in Engineering* 2015; **101**:774–808.
25. Oesterle B, Ramm E, Bischoff M. A shear deformable, rotation-free isogeometric shell formulation. *Computer Methods in Applied Mechanics and Engineering* 2016; **307**:235–255.
26. Duong TX, Roohbakhshan F, Sauer RA. A new rotation-free isogeometric thin shell formulation and a corresponding continuity constraint for patch boundaries. *Computer Methods in Applied Mechanics and Engineering* 2017; **316**:43–83.
27. Leonetti L, Magisano D, Madeo A, Garcea G, Kiendl J, Reali A. A simplified kirchhoff-love large deformation model for elastic shells and its effective isogeometric formulation. *Computer Methods in Applied Mechanics and Engineering* 2019; **354**:369–396.
28. Zou Z, Scott M, Miao D, Bischoff M, Oesterle B, Dornisch W. An isogeometric Reissner-Mindlin shell element based on Bézier dual basis functions: Overcoming locking and improved coarse mesh accuracy. *Computer Methods in Applied Mechanics and Engineering* 2020; **370**:113 283.
29. Breitenberger M, Apostolatos A, Philipp B, Wüchner R, Bletzinger KU. Analysis in computer aided design: Nonlinear isogeometric B-Rep analysis of shell structures. *Computer Methods in Applied Mechanics and Engineering* 2015; **284**:401–457.
30. Lei Z, Gillot F, Jezequel A. A C0 / G1 multiple patches connection method in isogeometric analysis. *Applied Mathematical Modelling* 2015; **39(15)**:4405–4420, doi:10.1016/j.apm.2014.12.055.
31. Kiendl J, Bazilevs Y, Hsu MC, Wüchner R, Bletzinger KU. The bending strip method for isogeometric analysis of Kirchhoff–Love shell structures comprised of multiple patches. *Computer Methods in Applied Mechanics and Engineering* 2010; **199(37-40)**:2403–2416.

32. Horger T, Reali A, Wohlmuth B, Wunderlich L. A hybrid isogeometric approach on multi-patches with applications to kirchhoff plates and eigenvalue problems. *Computer Methods in Applied Mechanics and Engineering* 2019; **348**:396–408.

33. Kamensky D, Evans J, Hsu MC, Bazilevs Y. Projection-based stabilization of interface lagrange multipliers in immersogeometric fluid–thin structure interaction analysis, with application to heart valve modeling. *Computers & Mathematics with Applications* 2017; **74(9)**:2068–2088, doi:10.1016/j.camwa.2017.07.006.

34. Sommerwerk K, Woidt M, Haupt M, Horst P. Reissner-mindlin shell implementation and energy conserving isogeometric multi-patch coupling: Iga shell implementation and multi-patch coupling. *International Journal for Numerical Methods in Engineering* 2017; **109(7)**:982–1012, doi:10.1002/nme.5316.

35. Guo Y, Heller J, Hughes T, Ruess M, Schillinger D. Variationally consistent isogeometric analysis of trimmed thin shells at finite deformations, based on the step exchange format. *Computer Methods in Applied Mechanics and Engineering* 2018; **336**:39–79.

36. Guo Y, Ruess M. Nitsche's method for a coupling of isogeometric thin shells and blended shell structures. *Computer Methods in Applied Mechanics and Engineering* 2015; **284**:881–905.

37. Guo Y, Zou Z, Ruess M. Isogeometric multi-patch analyses for mixed thin shells in the framework of non-linear elasticity. *Computer Methods in Applied Mechanics and Engineering* 2021; **380**(49–52):113 771.

38. Nguyen-Thanh N, Zhou K, Zhuang X, Areias P, Nguyen-Xuan H, Bazilevs Y, Rabczuk T. Isogeometric analysis of large-deformation thin shells using RHT-splines for multiple-patch coupling. *Computer Methods in Applied Mechanics and Engineering* 2017; **316**:1157–1178, doi:10.1016/j.cma.2016.12.002.

39. Harari I, Grosu E. A unified approach for embedded boundary conditions for fourth-order elliptic problems. *International Journal for Numerical Methods in Engineering* 2015; **104**(7):655–675.

40. Ruess M, Schillinger D, Özcan AI, Rank E. Weak coupling for isogeometric analysis of non-matching and trimmed multi-patch geometries. *Computer Methods in Applied Mechanics and Engineering* 2014; **269**:46–71.

41. Nguyen V, Kerfriden P, Brino M, Bordas S, Bonisoli E. Nitsche's method for two and three dimensional NURBS patch coupling. *Computational Mechanics* 2014; **53(6)**:1163–1182, doi:10.1007/s00466-013-0955-3.

42. Du X, Zhao G, Wang W. Nitsche method for isogeometric analysis of reissner-mindlin plate with non-conforming multi-patches. *Computer Aided Geometric Design* 2015; **35-36**:121–136.

43. Bouclier R, Passieux JC. A nitsche-based non-intrusive coupling strategy for global/local isogeometric structural analysis. *Computer Methods in Applied Mechanics and Engineering* 2018; **340**:253–277.

44. Apostolatos A, Schmidt R, Wüchner R, Bletzinger KU. A Nitsche-type formulation and comparison of the most common domain decomposition methods in isogeometric analysis. *International Journal for Numerical Methods in Engineering* 2014; **97**:473–504.

45. Shojaee S, Valizadeh N, Izadpanah E, Bui T, Vu TV. Free vibration and buckling analysis of laminated composite plates using the NURBS-based isogeometric finite element method. *Composite Structures* 2012; **94(5)**:1677–1693.

46. Thai CH, Nguyen-Xuan H, Nguyen-Thanh N, Le TH, Nguyen-Thoi T, Rabczuk T. Static, free vibration, and buckling analysis of laminated composite Reissner-Mindlin plates using NURBS-based isogeometric approach. *International Journal for Numerical Methods in Engineering* 2012; **91(6)**:571–603.

47. Guo Y, Ruess M, Gürdal Z. A contact extended isogeometric layerwise approach for the buckling analysis of delaminated composites. *Composite Structures* 2014; **116**:55–66.

48. Yu T, Yin S, Bui T, Xia S, Tanaka S. NURBS-based isogeometric analysis of buckling and free vibration problems for laminated composites plates with complicated cutouts using a new simple FSDT theory and level set method. *Thin-Walled Structures* 2016; **101**:141–156.

49. Guo Y, Do H, Ruess M. Isogeometric stability analysis of thin shells: from simple geometries to engineering models. *International Journal for Numerical Methods in Engineering* 2019; **118**:433–458.

50. Hao P, Wang Y, Tang H, Feng S, Wang B. A nurbs-based degenerated stiffener element for isogeometric static and buckling analysis. *Computer Methods in Applied Mechanics and Engineering* 2022; **398**:115 245.

51. Oesterle B, Geiger F, Forster D, Fröhlich M, Bischoff M. A study on the approximation power of NURBS and the significance of exact geometry in isogeometric pre-buckling analysis of shells. *Computer Methods in Applied Mechanics and Engineering* 2022; **397**:115 144.

52. Le-Manh T, Lee J. Postbuckling of laminated composite plates using NURBS-based isogeometric analysis. *Composite Structures* 2014; **109**:286–293.

53. Luo K, Liu C, Tian Q, Hu H. An efficient model reduction method for buckling analyses of thin shells based on iga. *Computer Methods in Applied Mechanics and Engineering* 2016; **309**:243–268.

54. Benson D, Hartmann S, Bazilevs Y, Hsu M, Hughes T. Blended isogeometric shells. *Computer Methods in Applied Mechanics and Engineering* 2013; **255**:133–146.

55. Leidinger L, Breitenberger M, Bauer A, Hartmann S, Wˊuchner R, Bletzinger KU, Duddeck F, Song L. Explicit dynamic isogeometric B-Rep analysis of penalty-coupled trimmed NURBS shells. *Computer Methods in Applied Mechanics and Engineering* 2019; **351**:891–927.

56. Magisano D, Leonetti L, Garcea G. Unconditional stability in large deformation dynamic analysis of elastic structures with arbitrary nonlinear strain measure and multi-body coupling. *Computer Methods in Applied Mechanics and Engineering* 2022; **393**:114 776.

57. Occelli M, Elguedj T, Bouabdallah S, Morançay L. LR B-Splines implementation in the Altair Radiouss$^{\text{tm}}$ solver for explicit dynamics Isogeometric Analysis. *Advances in Engineering Software* 2019; **131**:166–185.

58. Stanič A, Brank B, Korelc J. On path-following methods for structural failure problems. *Computational Mechanics* 2016; **58**:281–306.

59. Stanić A, Brank B. A path-following method for elasto-plastic solids and structures based on control of plastic dissipation and plastic work. *Finite Elements in Analysis and Design* 2017; **123**:1–8.

60. Simitses G, Sheinman I. Dynamic buckling of shell structures: concepts and applications. *Acta Astronautica* 1982; **9(3)**:179–182.

61. Combescure A. Static and dynamic buckling of large thin shells – design procedure, computation tools, physical understanding of the mechanisms. *Nuclear Engineering and Design* 1986; **92**:339–354.

36

62. Hilburger M, Waas A, Starnes Jr J. Modeling the dynamics response and establishing post-buckling/post snap-thru equilibrium of discrete structures via a transient analysis. *Journal of Applied Mechanics* 1997; **64**:590–595.
63. Saigal S, Yang T, Kapania R. Dynamic buckling of imperfection-sensitive shell structures. *Journal of Aircraft* 2012; **24**:718–724.
64. Lavrenčič M, Brank B. Simulation of shell buckling by implicit dynamics and numerically dissipative schemes. *Thin-Walled Structures* 2018; **132**:682–699.
65. Newmark N. A method of computation for structural dynamics. *Journal of the Engineering Mechanics Division* 1959; **85**:67–94.
66. Hilber H, Hughes T, Taylor R. Improved numerical dissipation for time integration algorithms in structural dynamics. *Earthquake Engineering Structural Dynamics* 1977; **5**:283–292.
67. Wood W, Bossak M, Zienkiewicz O. An alpha-modification of newmark method. *International Journal for Numerical Methods in Engineering* 1980; **15**:1562–1566.
68. Chung J, Hulbert G. A time integration algorithm for structural dynamics with improved numerical dissipation – the generalized-alpha method. *Journal of Applied Mechanics* 1993; **60**:371–375.
69. Armero F, Romero I. On the formulation of high-frequency dissipative time-stepping algorithms for nonlinear dynamics. Part I: low-order methods for two model problems and nonlinear elastodynamics. *Computer Methods in Applied Mechanics and Engineering* 2001; **190**:2603–2649.
70. Betsch P, Janz A. An energy-momentum consistent method for transient simulations with mixed-finite elements developed in the framework of geometrically exact shells. *International Journal for Numerical Methods in Engineering* 2016; **108**:423–455.
71. Brank B, Briseghella L, Tonello N, Damjanić F. On non-linear dynamics of shells: implementation of energy-momentum conserving algorithm for a finite rotation shell model. *International Journal for Numerical Methods in Engineereing* 1998; **42**:409–442.
72. Kuhl D, Crisfield M. Energy conserving and decaying algorithms in non-linear structural dynamics. *International Journal for Numerical Methods in Engineering* 1999; **45**:569–599.
73. Simo J, Tarnow N. A new energy and momentum conserving algorithm for the nonlinear dynamics of shells. *International Journal for Numerical Methods in Engineering* 1994; **37**:2527–2549.
74. Simo J, Rifai M, Fox D. On a stress resultant geometrically exact shell model. Part VI: Conserving algorithms for non-linear dynamics. *International Journal for Numerical Methods in Engineering* 1992; **34**:117–164.
75. Kuhl D, Ramm E. Generalized Energy-Momentum Method for non-linear adaptive shell dynamics. *Computer Methods in Applied Mechanics and Engineering* 1999; **178**:343–366.
76. Vu-Quoc L, Tan X. Optimal solid shells for non-linear analyses of multilayer composites. II. Dynamics. *Computer Methods in Applied Mechanics and Engineering* 2003; **192**:1017–1059.
77. Armero F, Petocz E. Formulation and analysis of conserving algorithms for frictionless dynamic contact/impact problems. *Computer Methods in Applied Mechanics and Engineering* 1998; **158**:269–300.
78. Armero F, Romero I. On the formulation of high-frequency dissipative time-stepping algorithms for nonlinear dynamics. Part II: second-order methods. *Computer Methods in Applied Mechanics and Engineering* 2001; **190**:6783–6824.
79. Gebhardt C, Romero I, Rolfes R. A new conservative/dissipative time integration scheme for nonlinear mechanical systems. *Computational Mechanics* 2020; **65**:405–427.
80. Piegl L, Tiller W. *The NURBS book - Monographs in Visual Communication*. Springer-Verlag Publishing Company, Inc.: Heidelberg, 1997.
81. Ruess M, Schillinger D, Bazilevs Y, Varduhn V, Rank E. Weakly enforced essential boundary conditions for NURBS-embedded and trimmed NURBS geometries on the basis of the finite cell method. *International Journal for Numerical Methods in Engineering* 2013; **95**:811–846.
82. Floater MS. Parametrization and smooth approximation of surface triangulations. *Computer Aided Geometric Design* 1997; **14**(3):231–250.
83. Guo Y. Complete Animations of Buckling Processes. *Available from: https://sites.google.com/site/nuaayujieguo/research/structural-stability* 2022; .
84. Kobayashi T, Mihara Y, Fujii F. Path-tracing analysis for post-buckling process of elastic cylindrical shells under axial compression. *Thin-Walled Structures* 2012; **61**:180–187.
85. Yamaki N. *Elastic Stability of Circular Cylindrical Shells*. North-Holland, Netherlands, 1984.
86. Timoshenko S. *Theory of elastic stability*. McGraw-Hill, New York, 1936.
87. Hibbit, Karlsson, Sorensen. *ABAQUS/Standard Analysis User's Manual*. Hibbit, Karlsson, Sorensen Inc.: USA, 2007.
88. Arbocz J, Abramovich H. The initial imperfection data bank at the Delft University of Technology, Part I. *Technical Report Technical Report LR-290*, Delft University of Technology 1979.